Monthly Notices
of the
ROYAL ASTRONOMICAL SOCIETY

MNRAS **504,** 2577–2602 (2021) doi:10.1093/mnras/stab907

A unicorn in monoceros: the 3 $M_\odot$ dark companion to the bright, nearby red giant V723 Mon is a non-interacting, mass-gap black hole candidate

T. Jayasinghe [1,2]★ K. Z. Stanek,[1,2] Todd A. Thompson [1,2] C. S. Kochanek [1,2] D. M. Rowan [1,2] P. J. Vallely [1,2] K. G. Strassmeier,[3] M. Weber,[3] J. T. Hinkle [4] F.-J. Hambsch,[5,6,7] D. V. Martin,[1]† J. L. Prieto,[8,9] T. Pessi,[8] D. Huber,[4] K. Auchettl,[10,11,12] L. A. Lopez,[1,2] I. Ilyin,[3] C. Badenes,[13] A. W. Howard,[14] H. Isaacson[15,16] and S. J. Murphy [17,18]

Affiliations are listed at the end of the paper

Accepted 2021 March 26. Received 2021 March 16; in original form 2021 January 6

ABSTRACT

We report the discovery of the closest known black hole candidate as a binary companion to V723 Mon. V723 Mon is a nearby ($d \sim 460$ pc), bright ($V \simeq 8.3$ mag), evolved ($T_{\rm eff,\,giant} \simeq 4440$ K, and $L_{\rm giant} \simeq 173$ $L_\odot$) red giant in a high mass function, $f(M) = 1.72 \pm 0.01$ $M_\odot$, nearly circular binary ($P = 59.9$ d, $e \simeq 0$). V723 Mon is a known variable star, previously classified as an eclipsing binary, but its All-Sky Automated Survey, Kilodegree Extremely Little Telescope, and Transiting Exoplanet Survey Satellite light curves are those of a nearly edge-on ellipsoidal variable. Detailed models of the light curves constrained by the period, radial velocities, and stellar temperature give an inclination of $87.0^{\circ\,+1.7^\circ}_{-1.4^\circ}$, a mass ratio of $q \simeq 0.33 \pm 0.02$, a companion mass of $M_{\rm comp} = 3.04 \pm 0.06$ $M_\odot$, a stellar radius of $R_{\rm giant} = 24.9 \pm 0.7$ $R_\odot$, and a giant mass of $M_{\rm giant} = 1.00 \pm 0.07$ $M_\odot$. We identify a likely non-stellar, diffuse veiling component with contributions in the B and V band of ∼63 per cent and ∼24 per cent, respectively. The SED and the absence of continuum eclipses imply that the companion mass must be dominated by a compact object. We do observe eclipses of the Balmer lines when the dark companion passes behind the giant, but their velocity spreads are low compared to observed accretion discs. The X-ray luminosity of the system is $L_{\rm X} \simeq 7.6 \times 10^{29}$ ergs s^{-1}, corresponding to $L/L_{\rm edd} \sim 10^{-9}$. The simplest explanation for the massive companion is a single compact object, most likely a black hole in the 'mass gap'.

Key words: binaries: spectroscopic – stars: black holes – stars: individual: V723 Mon.

1 INTRODUCTION

The discovery and characterization of neutron stars (NSs) and black holes (BHs) in the Milky Way is crucial for understanding core-collapse supernovae and massive stars. This is inherently challenging, partly because isolated BHs are electromagnetically dark and partly because compact object progenitors (OB stars) are rare. To date, most mass measurements for NSs and BHs come from pulsar and accreting binary systems selected from radio, X-ray, and gamma-ray surveys (see e.g. Liu, van Paradijs & van den Heuvel 2006; Champion et al. 2008; Özel et al. 2010; Farr et al. 2011), and from the LIGO/Virgo detections of merging systems (see e.g. Abbott et al. 2016, 2017). Interacting and merging systems are, however, a biased sampling of compact objects. A more complete census is needed to constrain their formation pathways.

One important component of such a census is to identify non-interacting compact objects in binaries around luminous companions. By their very nature, interacting BHs only sample a narrow range of binary configurations, and almost the entire parameter space of binaries with BHs that are non-interacting remains unexplored. Interacting compact object binaries are only active for relatively short periods of time, so most systems are quiescent or non-interacting. The discovery and characterization of these non-interacting BHs are important for understanding the birth mass distribution of BHs and their formation mechanisms.

With advances in time-domain astronomy and precision *Gaia* astrometry (Gaia Collaboration 2018), a significant number of these systems should be discoverable. For example, Breivik, Chatterjee & Larson (2017) estimated that $\sim 10^3 - 10^4$ non-interacting BHs are detectable using astrometry from *Gaia*. Similarly, Shao & Li (2019) used binary population synthesis models to estimate that there are $\sim 10^3$ detached non-interacting BHs in the Milky Way, with 10^2 of these systems having luminous companions that are brighter than $G \sim 20$ mag.

Thompson et al. (2019) recently discovered the first low-mass ($M_{\rm BH} \simeq 3.3^{+2.8}_{-0.7}$ $M_\odot$), non-interacting BH candidate in the field. It is in a circular orbit with $P_{\rm orb} \sim 83$ d around a spotted giant star. Other non-interacting BH candidates have been discovered in globular clusters: one by Giesers et al. (2018) in NGC 3201 (minimum BH mass $M_{\rm BH} = 4.36 \pm 0.41$ $M_\odot$), and two by Giesers et al. (2019) in NGC 3201 ($M_{\rm BH}\sin(i) = 7.68 \pm 0.50$ $M_\odot$ and $M_{\rm BH}\sin(i) = 4.4 \pm 2.8$ $M_\odot$). While obviously interesting in their own right, these globular cluster systems likely have formation mechanisms that are very different from those of field BH binaries.

★ E-mail: jayasinghearachchilage.1@osu.edu
† Fellow of the Swiss National Science Foundation

Other claims for non-interacting BH systems have been ruled out. For example, LB-1, which was initially thought to host an extremely massive stellar BH ($M_{\rm BH} \simeq 68^{+11}_{-3}$ M$_\odot$, Liu et al. 2019), was later found to have a much less massive companion that was not necessarily a compact object (see e.g. Abdul-Masih et al. 2020; El-Badry & Quataert 2020; Irrgang et al. 2020; Shenar et al. 2020). Similarly, the naked-eye star HR 6819 was claimed to be a triple system with a detached BH with $M_{\rm BH} = 6.3 \pm 0.7$ M$_\odot$ (Rivinius et al. 2020), but was later argued to contain a binary system with a rapidly rotating Be star and a slowly rotating B star (Bodensteiner et al. 2020; El-Badry & Quataert 2021).

Here, we discuss our discovery that the bright red giant V723 Mon has a dark, massive companion that is a good candidate for the closest known BH. We discuss the current classification of this system in Section 2, and describe the archival data and new observations used in our analysis in Section 3. In Section 4, we analyse photometric and spectroscopic observations to derive the parameters of the binary system and the red giant secondary. In Section 5, we discuss the nature of the dark companion. We present a summary of our results in Section 6.

2 V723 MON

V723 Mon (HD 45762, SAO 133321, TIC 43077836) is a luminous ($m_V \simeq 8.3$) red-giant[1] in the Monoceros constellation with J2000 coordinates $(\alpha, \delta) = (97.269410^\circ, -5.572286^\circ)$. It was classified as a likely long period variable in the General Catalogue of Variable Stars (GCVS; Kazarovets et al. 1999) after it was identified as a variable source in the *Hipparcos* catalogue with period P = 29.97 d (ESA 1997). Subsequently, the All-Sky Automated Survey (ASAS; Pojmanski 1997, 2002) classified it as a contact/semidetached binary with P = 59.87 d. The Variable Star Index (VSX; Watson, Henden & Price 2006) presently lists it as an eclipsing binary of the β-Lyrae type (EB) with P = 59.93 d.

V723 Mon has a well determined spectroscopic orbit and is included in the the Ninth Catalogue of Spectroscopic Binary Orbits (Pourbaix et al. 2004). In particular, Griffin (2010) identified V723 Mon as a single-lined spectroscopic binary (SB1) with a nearly circular $P \sim 60$ d orbit. Strassmeier et al. (2012; hereafter S12) refined the orbit to $P_{\rm orb} = 59.9363 \pm 0.0016$ d and $e_{\rm orb} \simeq 0.0150 \pm 0.0009$ using a large number of high precision RV measurements from STELLA (Weber et al. 2008). S12 also argue that this is the outer orbit of a triple system, and that the more massive (inner) component is an SB1 consisting of another giant star and an unseen companion with a period $P_{\rm inner} \simeq P_{\rm outer}/3$. Griffin (2014; hereafter G14) was unable to find a spectral feature indicative of a second companion in their cross-correlation functions. G14 discusses several peculiarities in the S12 RV solution. In particular, the radial velocity (RV) curve associated with the second component is unusual in structure compared to any other system characterized by S12 and a triple system with this period ratio would almost certainly be dynamically unstable.

The most striking feature of the well-measured 60 day RV curve is its large mass function of

$$f(M) = \frac{P_{\rm orb} K^3 (1-e^2)^{3/2}}{(2\pi G)} = \frac{M^3_{\rm comp} \sin^3 i}{(M_{\rm giant} + M_{\rm comp})^2} \simeq 1.73\,{\rm M}_\odot, \quad (1)$$

given $P_{\rm orb} = 59.9363$ d, $e = 0.015$ and $K = 65.45$ km s^{-1} from S12. If the observed giant has a mass of $M_{\rm giant} \sim 1$ M$_\odot$, the mass function implies a massive companion with a minimum mass of $M_{\rm comp} \sim 3$ M$_\odot$. Since the observed light is clearly dominated by the giant and the companion has to be both much less luminous and significantly more massive than the giant, V723 Mon is a prime candidate for a non-interacting, compact object binary. This realization led us to investigate V723 Mon in detail as part of a larger project to identify non-interacting, compact object binaries.

3 OBSERVATIONS

Here, we present observations, both archival and newly acquired, that are used in our analysis of V723 Mon.

3.1 Distance, kinematics, and extinction

In *Gaia* EDR3 (Gaia Collaboration 2020), V723 Mon is `source_id` = 3104145904761393408. Its EDR3 parallax of $\varpi_{\rm EDR3} = 2.175 \pm 0.033$ mas implies a distance of $d = 1/\varpi = 460 \pm 7$ pc. This is little changed from its *Gaia* DR2 parallax of $\varpi_{\rm DR2} = 1.9130 \pm 0.0563$ mas. At these distances, there is little difference between $d = 1/\varpi = 519 \pm 15$ pc (for DR2) and the more careful estimate of $d = 515.6^{+15.6}_{-14.6}$ pc by Bailer-Jones et al. (2018). The astrometric solution has significant excess noise of $\Delta = 0.22$ mas, which is not surprising given that the motion of the giant should be ∼0.8 mas. However, its renormalized unit weight error of 1.39, while larger than unity, is not indicative of problems in the parallax. We adopt a distance of $d = 460$ pc for the remainder of the paper. The distance uncertainties are unimportant for our analysis.

V723 Mon has Galactic coordinates $(l, b) \simeq (215.372^\circ, -7.502^\circ)$, close to the Galactic disc, but away from the Galactic centre. At the EDR3 distance, V723 Mon is ∼32 pc below the mid-plane. Its proper motion in EDR3 is $\mu_\alpha = -1.347 \pm 0.032$ mas yr^{-1}, and $\mu_\delta = 16.140 \pm 0.031$ mas yr^{-1}. Combining this with the systemic RV from Section 4.2 and the definition of the local standard of rest (LSR) from Schönrich, Binney & Dehnen (2010), the 3D space motion of V723 Mon relative to the LSR as $(U, V, W)_{\rm LSR} = (-10.8 \pm 4.3, 36.9 \pm 5.3, 20.1 \pm 3.4)$ km s^{-1} using `BANYAN` (Gagné et al. 2018) for the calculations. We calculated the thin disc, thick disc, and halo membership probabilities based on the *UVW* velocities following Ramírez, Allende Prieto & Lambert (2013) to obtain P(thin) ≃ 97 per cent, P(thick) ≃ 3 per cent, and P(halo) ≃ 0 per cent, respectively. This suggests that this system is a kinematically normal object in the thin disc.

Gaia DR2 (Gaia Collaboration 2018) also reports a luminosity $L_{\rm Gaia} = 165.5 \pm 6.5$ L$_\odot$, temperature $T_{\rm eff,Gaia} = 4690^{+40}_{-30}$ K, and radius $R_{\rm Gaia} = 19.5^{+0.2}_{-0.4}$ R$_\odot$, for the star that are consistent with an evolved red giant. While *Gaia* DR2 does not report a value for the reddening towards V723 Mon, Gontcharov & Mosenkov (2017) reports $E(B-V) \simeq 0.10$. The three-dimensional dust maps of Green et al. (2019) give $E(B-V) \simeq 0.10 \pm 0.04$ at the *Gaia* distance, consistent with this estimate.

3.2 Light curves

We analysed well-sampled light curves from the ASAS and the Kilodegree Extremely Little Telescope (KELT), a densely sampled but phase-incomplete light curve from the Transiting Exoplanet Survey Telescope (*TESS*), BVR_cI_c light curves from the Remote Observatory Atacama Desert (ROAD) and a sparse ultraviolet (UV) light curve from the Neil Gehrels Swift Observatory.

[1] V723 Mon has previously been assigned a spectral type of G0 II (Houk & Swift 2000), however, in this work we find that it is more consistent with a K0/K1 III spectral type.

ASAS (Pojmanski 1997, 2002) obtained a *V*-band light curve of V723 Mon spanning from 2000 November to 2009 December (∼54 complete orbits). We selected 580 epochs with `GRADE = A` or `GRADE = B` for our analysis. V723 Mon clearly varies in the ASAS light curve, with two equal maxima but two unequal minima, when phased with the orbital period from S12. We determined the photometric period using the `Period04` software (Lenz & Breger 2005). The dominant ASAS period of $P_{\rm ASAS} \simeq 29.9674 \pm 0.0138$ d corresponds to $P_{\rm orb}/2$. Once the ASAS light curve was whitened using a sinusoid, we find an orbital period of

$$P_{\rm orb,ASAS} = 59.9863 \pm 0.0551 \,{\rm d}, \quad (2)$$

which agrees well with the spectroscopic periods from S12 and G14. Unfortunately, V723 Mon is saturated in the Automated Survey for SuperNovae (ASAS-SN; Shappee et al. 2014; Kochanek et al. 2017) images, and we could not use it to extend the time span of the *V*-band data.

The KELT (Pepper et al. 2007) light curve contains 1297 epochs that we retrieved from the Exoplanet Archive.[2] The KELT R_K filter can be considered as a very broad Johnson *R*-band filter (Siverd et al. 2012). However, there can be significant colour corrections compared to a standard Johnson *R*-band filter for very blue and very red stars (Pepper et al. 2007; Siverd et al. 2012). KELT observations were made between 2010 September and 2015 February (∼26 complete orbits). The dominant period in the KELT data ($P_{\rm KELT} \simeq 29.9682 \pm 0.0279$ d) again corresponds to $P_{\rm orb}/2$. We find an orbital period of

$$P_{\rm orb,KELT} = 60.0428 \pm 0.1121 \,{\rm d}. \quad (3)$$

The difference between the ASAS and KELT photometric period estimates is not statistically significant.

V723 Mon (`TIC 43077836`) was observed by *TESS* (Ricker et al. 2015) in Sector 6, and the 27 d of observations correspond to [0.46, 0.82] in orbital phase where the phase of the RV maximum is 0.75. V723 Mon was also observed in Sector 33, with the observations spanning [0.94, 0.36] in orbital phase. We analysed the *TESS* data using the adaptation of the ASAS-SN image subtraction pipeline for analyzing *TESS* full-frame images described in Vallely et al. (2021). While this pipeline produces precise differential flux light curves, the large pixel scale of *TESS* makes it difficult to obtain reliable measurements of the reference flux of a given source. We normalized the light curve to have the reference *TESS*-band magnitude of 7.26 in the *TESS* Input Catalogue (Stassun et al. 2019). Conveniently, the mean of the Sector 6 observations is approximately the mean for a full orbital cycle (see Fig. 5). We use a zero-point of 20.44 electrons (*TESS* Instrument Handbook[3]). The light curve does not include epochs where the observations were compromised by the spacecraft's momentum dump maneuvers.

We obtained BVR_cI_c light curves at the ROAD (Hambsch 2012). All observations were acquired through Astrodon Photometric filters with an Orion Optics, UK Optimized Dall Kirkham 406/6.8 telescope and a FLI 16803 CCD camera. Twilight sky-flat images were used for flat-field corrections. Reductions were performed with the `MAXIM DL` program,[4] and the photometry was carried out using the `LesvePhotometry` program.[5]

We obtained Swift UVOT (Roming et al. 2005) images in the *UVM*2 (2246 Å) band (Poole et al. 2008) through the Target of Opportunity (ToO) program (Target ID number 13777). We only obtained images in the *UVM*2 band because the *Swift UVW*1 and *UVW*2 filters have significant red leaks that make them unusable in the presence of the emission from the cool giant, and the star is too bright to obtain images in the optical UVOT filters. Each epoch of UVOT data includes multiple observations per filter, which we combined using the `uvotimsum` package. We then used `uvotsource` to extract source counts using a 5.″0 radius aperture centred on the star. We measured the background counts using a source-free region with radius of 40.″0 and used the most recent calibrations (Poole et al. 2008; Breeveld et al. 2010) and taking into account the recently released update to the sensitivity correction for the Swift UV filters.[6] The Swift *UVM*2 observations are summarized in Table 6. We report the median and standard deviation of these *UVM*2 observations in Table 1.

3.3 Radial velocities

We used two sets of RV measurements. The first set, from Griffin (2014), was obtained between 2008 December and 2013 November as part of the Cambridge Observatory RV Program and span 1805 d. The median RV error for this data set is $\sim$0.80 km s^{-1}. These 41 RV epochs were retrieved from the Ninth Catalogue of Spectroscopic Binary Orbits (SB9; Pourbaix et al. 2004),[7] converting the reported epochs to Barycentric Julian Dates (BJD) on the TDB system (Eastman, Siverd & Gaudi 2010) using `barycorrpy` (Kanodia & Wright 2018).

The second set of RV data consists of 100 epochs obtained by S12 with the high resolution ($R \approx 55000$) STELLA spectrograph. STELLA spectra have a wavelength coverage of 390–880 nm and a spectral resolution of 0.12 Å at 650 nm. Spectra were obtained between 2006 November and 2010 April, spanning a baseline of 1213 d. The spectra were reduced following the standard procedures described in Strassmeier et al. (2012) and Weber et al. (2008). Of the 100 spectra, 75 had S/N > 30 near 650 nm. There were 87 epochs with good RV measurements for the giant and the median RV error is $\sim$0.19 km s^{-1}. The STELLA RV measurements are listed in Table 7.

3.4 Additional spectra

To better understand the V723 Mon system, and to test for possible systematic errors, we obtained a number of additional high- and medium-resolution spectra These observations are summarized in Table 8. Using the HIRES instrument (Vogt et al. 1994) on Keck I, we obtained seven spectra with $R \approx 60000$ between 2020 October 20 and 2020 December 26 using the standard California Planet Search (CPS) set-up (Howard et al. 2010). The exposure times ranged from 35 to 60 s. We also obtained a very high resolution ($R \approx 220000$) spectrum on 2020 November 29 using the Potsdam Echelle Polarimetric and Spectroscopic Instrument (PEPSI; Strassmeier et al. 2015) on the Large Binocular Telescope. We used the 100 µm fiber and six cross-dispersers (CD). The data were processed as described in Strassmeier, Ilyin & Steffen (2018). The total integration time was 90 min, and the combined spectrum covers the entire wavelength range accessible to PEPSI (3840−9070 Å). The spectrum has a signal-to-noise ratio

[2] https://exoplanetarchive.ipac.caltech.edu/
[3] https://archive.stsci.edu/files/live/sites/mast/files/home/missions-and-data/active-missions/⟨0:italic ⟩TESS⟨/0:italic⟩/_documents/⟨0:italic ⟩TESS⟨/0:italic⟩_Instrument_Handbook_v0.1.pdf
[4] http://www.cyanogen.com
[5] http://www.dppobservatory.net/
[6] https://www.swift.ac.uk/analysis/uvot/index.php
[7] https://sb9.astro.ulb.ac.be/DisplayFull.cgi?3936 + 1

Table 1. Multiband photometry measurements used in the construction of the SED for V723 Mon. Luminosities in each band are calculated assuming a nominal distance of $d \simeq 460$ pc.

Filter	Magnitude	σ	F_λ (ergs s^{-1} cm^{-2} Å^{-1})	λL_λ ($L_\odot$)	Reference
Swift UVM2	14.11	0.07	1.0×10^{-14}	0.15	This work
SkyMapper u	10.30	0.01	2.5×10^{-13}	5.7	Onken et al. (2019)
SkyMapper v	9.74	0.01	7.1×10^{-13}	18.1	Onken et al. (2019)
Johnson B	9.24	0.05	1.3×10^{-12}	36.5	Henden et al. (2018)
Johnson V	8.30	0.04	1.7×10^{-12}	61.8	Henden et al. (2018)
Sloan g'	8.73	0.01	1.6×10^{-12}	49.1	Henden et al. (2018)
Sloan r'	7.87	0.12	2.0×10^{-12}	81.2	Henden et al. (2018)
Sloan i'	7.49	0.14	1.9×10^{-12}	94.9	Henden et al. (2018)
Sloan z'	7.36	0.05	1.1×10^{-12}	77.8	Henden et al. (2018)
2MASS J	6.26	0.03	9.8×10^{-13}	80.2	Skrutskie et al. (2006)
2MASS H	5.58	0.03	6.7×10^{-13}	73.3	Skrutskie et al. (2006)
2MASS K_s	5.36	0.02	3.1×10^{-13}	43.7	Skrutskie et al. (2006)
WISE W1	5.28	0.16	6.3×10^{-14}	14.0	Wright et al. (2010)
WISE W2	5.10	0.07	2.2×10^{-14}	6.7	Wright et al. (2010)
WISE W3	5.01	0.02	6.5×10^{-16}	0.5	Wright et al. (2010)
WISE W4	4.82	0.04	6.0×10^{-17}	0.1	Wright et al. (2010)

(S/N) of 70 in the wavelength range 4265−4800 Å (CD2) and S/N = 260 in the range 7419−9070 Å (CD6).

Using the medium resolution ($R \approx 2000$) Multi-Object Double Spectrographs mounted on the twin 8.4 m Large Binocular Telescope (MODS1 and MODS2; Pogge et al. 2010), we obtained a series of spectra from 2020 November 18 to 22 as the dark companion moved into eclipse behind the observed giant. Exposure times were typically 15 s, but this was extended to 24 s for the November 22 observation to compensate for clouds. We used a 2.″4 wide slit to ensure that all the light was captured. We reduced these observations using a standard combination of the `modsccdred`[8] PYTHON package, and the `modsidl` pipeline.[9] The blue and red channels of both spectrographs were reduced independently, and the final MODS spectrum for each night was obtained by averaging the MODS1 and MODS2 spectra. The best weather conditions during this observing run occurred on Nov 20. The HIRES, PEPSI, and MODS observations are summarized in Table 8.

3.5 X-ray data

We analysed X-ray observations from the *Swift* X-Ray Telescope (XRT; Burrows et al. 2005) and *XMM–Newton* (Jansen et al. 2001). The XRT data were taken simultaneously with the *UVM*2 observations, with individual exposure times of 160 to 1015 seconds. Additionally, two longer ∼5 ks XRT exposures were taken on 2021-01-21 ($\phi \simeq 0.5$) and 2021-02-20 ($\phi \simeq 0$). In total, V723 Mon was observed with *Swift* XRT for 19865 s. All XRT observations were reprocessed using the *Swift* XRTPIPELINE version 0.13.2 and standard filter and screening criteria[10] and the most up-to-date calibration files. To increase the signal to noise of our observations, we combined all cleaned individual XRT observations using XSELECT version 2.4g. To place constraints on the presence of X-ray emission, we used a source region with a radius of 30 arcsec centred on the position of V723 Mon and a source-free background region with a radius of 150 arcsec located at RA = 06:28:53.1, Dec. = −05:38:49.6 (J2000).

We also retrieved archival *XMM–Newton* data obtained during a ∼10 ks observation of the nearby ultraluminous infrared galaxy IRAS 06269-0543 (Observation ID 0153100601; PI: N. Anabuki). However, V723 Mon is ∼12 arcmin off-axis in these observations, resulting in a non-optimal PSF with a 90 per cent enclosed energy radius of ∼1 arcmin. We reduced the data using the *XMM–Newton* Science System (SAS) Version 15.0.0 (Gabriel et al. 2004). We removed time intervals with proton flares or high background after identifying them by producing count-rate histograms using events with an energy between 10 and 12 keV. For the data reduction, we used the standard screening procedures and the FLAGS recommended in the current SAS analysis threads[11] and *XMM–Newton* Users Handbook.[12]

4 RESULTS

Here, we present our analyses of the observations described in Section 3. In Section 4.1, we characterize the red giant using its spectral energy distribution (SED) and spectra. In Section 4.2, we fit Keplerian models to the radial velocities and derive a spectroscopic orbit for V723 Mon. In Section 4.3, we model the ellipsoidal variations of the red giant using multiband light curves and the binary modelling tools `PHOEBE` and `ELC` to derive the masses of the red giant and the dark companion. We also derive limits on companion eclipse depths. In Section 4.4, we characterize the veiling component in this system. In Section 4.5, we place constraints on luminous stellar companions. In Section 4.6, we characterize the Balmer emission lines and their variability. In Section 4.7, we discuss the X-ray observations.

4.1 Properties of the red giant secondary

We characterized the red giant using both fits to its overall SED and analyses of the available spectra. For the SED, we used photometry from APASS DR10 (Henden et al. 2018), SkyMapper DR2 (Onken et al. 2019), 2MASS (Skrutskie et al. 2006), and AllWISE (Wright

[8] http://www.astronomy.ohio-state.edu/MODS/Software/modsCCDRed/
[9] http://www.astronomy.ohio-state.edu/MODS/Software/modsIDL/
[10] http://swift.gsfc.nasa.gov/analysis/xrt_swguide_v1_2.pdf
[11] https://www.cosmos.esa.int/web/XMM–Newton/sas-threads
[12] https://xmm-tools.cosmos.esa.int/external/xmm_user_support/documentation/uhb/

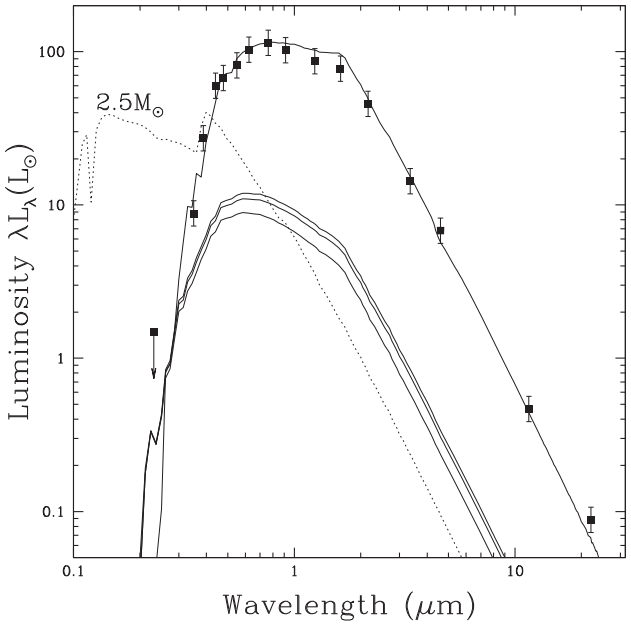

Figure 1. The best-fitting, extinction-corrected SED model for V723 Mon without considering veiling (see Section 4.4). The *Swift UVM2* detection (the arrow; see Table 1) is treated as an upper limit and the error bars are expanded to give $\chi^2/N_{\rm dof} \simeq 1$. The SEDs for a main-sequence companion of mass 1.29 $M_\odot$, an equal mass binary consisting of two main-sequence stars each with 0.99 $M_\odot$, and a binary with companion masses of 1.25 and 0.77 $M_\odot$ are also shown (see Section 4.5). These SEDs closely overlap and are hard to distinguish. As shown by the SED of a single 2.5 $M_\odot$ main-sequence star (dashed line), hotter stars are easily ruled out.

et al. 2010). We used the *Swift* UVM2 photometry only as an upper limit (Section 3.5). The compilation of the multiband photometry used in these fits are given in Table 1.

We fit the SED of V723 Mon using DUSTY (Ivezic & Elitzur 1997; Elitzur & Ivezić 2001) inside an MCMC wrapper (Adams & Kochanek 2015). We assumed foreground extinction due to $R_V = 3.1$ dust (Cardelli, Clayton & Mathis 1989) and used the ATLAS9 Castelli & Kurucz (2003) model atmospheres for the star. We assume that the source is at the *Gaia* EDR3 distance and used minimum luminosity uncertainties of 19 per cent for each band to obtain $\chi^2/N_{\rm dof} \simeq 1$. The expanded uncertainties needed to reach $\chi^2/N_{\rm dof} \simeq 1$ with respect to the reported photometric errors in each measurement are likely driven using single epoch photometry for a variable source plus any systematic problems in the models and photometry. We used a weak $T_{\rm eff,\,giant} = 4500 \pm 500$ K prior on the temperature and a prior of $E(B-V) = 0.10 \pm 0.04$ on the extinction from Green et al. (2019). The SED fit yields $T_{\rm eff,\,giant} \simeq 4440 \pm 90$ K, $L_{\rm giant} = 173 \pm 8\ L_\odot$, $R_{\rm giant} \simeq 22.2 \pm 0.8\ R_\odot$ and $E(B-V) \simeq 0.085 \pm 0.034$ mag. Fig. 1 shows the SED and the best-fitting model. The SED well constrains the temperature and is consistent with the extinction estimates. If we force the model to have smaller stellar radii, the goodness of fit worsens rapidly, from $\chi^2 = 13.6$ for the best fit to 20.3 for $R_{\rm giant} = 20\,R_\odot$ and 40.9 for $R_{\rm giant} = 18\,R_\odot$. Decreasing the radius forces the star to become hotter (4800 K for 18 $R_\odot$) to fit the SED at long wavelengths and more extincted to fit it at short wavelengths. Constraints on a stellar companion to the giant from the SED are discussed in Section 4.5.

The equivalent width (EW) of the Na I D doublet provides an independent estimate of the Galactic reddening towards V723 Mon (see e.g. Poznanski, Prochaska & Bloom 2012). Using the very high resolution PEPSI spectrum, we measure $\mathrm{EW(D_1)} = 125.1 \pm 12.0$ mÅ and $\mathrm{EW(D_2)} = 85.7 \pm 7.5$ mÅ. From the EW–$E(B-V)$ calibration in Poznanski et al. (2012), we find that $E(B-V) = 0.025 \pm 0.005$ mag. This is consistent with the low foreground extinction that was derived from the SED models and the Green et al. (2019) extinction maps.

All high-resolution spectra indicate that the giant is rapidly rotating. Strassmeier et al. (2012) derived a projected rotational velocity of $v_{\rm rot} \sin i = 16 \pm 2\,{\rm km\,s^{-1}}$ using the SES spectra. Griffin (2014) found a similar average $v_{\rm rot} \sin i \sim 15\,{\rm km\,s^{-1}}$ but noted that the values seemed to depend on the orbital phase and ranged from $v_{\rm rot} \sin i \sim 10\,{\rm km\,s^{-1}}$ to $v_{\rm rot} \sin i \sim 20\,{\rm km\,s^{-1}}$. We also find that $v_{\rm rot} \sin i$ varies from ∼17.6 to ∼21.7 $\rm km\,s^{-1}$ in the SES spectra. The HIRES CPS pipeline (Petigura 2015) reports $v_{\rm rot} \sin i = 21.6 \pm 1.0\,{\rm km\,s^{-1}}$, and we found $v_{\rm rot} \sin i = 17.9 \pm 0.4\,{\rm km\,s^{-1}}$ from the PEPSI spectrum using `iSpec` (Blanco-Cuaresma et al. 2014; Blanco-Cuaresma 2019). Assuming that the rotation of the giant is tidally synchronized with the orbit, the SES, PEPSI and HIRES measurements yield stellar radii of $R \sin i = 19.0 \pm 2.4\,R_\odot$, $R \sin i = 21.2 \pm 0.5\,R_\odot$, and $R \sin i = 25.6 \pm 1.2\,R_\odot$, respectively, consistent both with estimates from the SED and the radius derived for the giant from the `PHOEBE` models (Section 4.3). The match to the estimate of the radius from the SED indicates that $\sin i \simeq 1$ independent of the `PHOEBE` models.

To derive the surface temperature ($T_{\rm eff}$), surface gravity [$\log(g)$], and metallicity [(Fe/H)] of the giant, we use the spectral synthesis codes `FASMA` (Tsantaki et al. 2018; Tsantaki, Andreasen & Teixeira 2020) and `iSpec`. `FASMA` generates synthetic spectra based on the ATLAS-APOGEE atmospheres (Kurucz 1993; Mészáros et al. 2012) with `MOOG` (Sneden 1973) and outputs the best-fitting stellar parameters following a χ^2 minimization process. `iSpec` carries out a similar minimization process with synthetic spectra generated by `SPECTRUM` (Gray & Corbally 1994) and MARCS model atmospheres (Gustafsson et al. 2008). The line lists used in this process span the wavelength range from 480 to 680 nm. Since we are confident the companion should undergo eclipses (see Section 4.5), we fit the SES spectrum near conjunction ($0.48 \lesssim \phi \lesssim 0.52$) when any companion would be eclipsed by the giant. For the detailed fits, we fix the rotational velocity to the value of $v_{\rm rot} \sin i = 19.1 \pm 0.4\,{\rm km\,s^{-1}}$ found by `iSpec` for this spectrum.

For the `FASMA` fits, we initially keep the macroturbulent broadening ($v_{\rm mac}$) and the microturbulence ($v_{\rm micro}$) fixed at $v_{\rm mac} = 5\,{\rm km\,s^{-1}}$ and $v_{\rm mic} = 2\,{\rm km\,s^{-1}}$, but then allow them to be optimized once we have a reasonable fit. This fits yield $T_{\rm eff,\,giant} = 4480 \pm 50$ K, $\log(g) = 1.7 \pm 0.2$, and $\mathrm{[Fe/H]} = -1.1 \pm 0.1$. In the `iSpec` fits, $v_{\rm mic}$ was kept as a free parameter and we obtain similar results with $T_{\rm eff,\,giant} = 4570 \pm 60$ K, $\log(g) = 1.7 \pm 0.1$, $\mathrm{[Fe/H]} = -0.9 \pm 0.1$, $[\alpha/\mathrm{Fe}] = 0.7 \pm 0.1$, and $v_{\rm micro} = 0.6 \pm 0.1\,{\rm km\,s^{-1}}$. We adopt the parameters from `iSpec` as our standard. Fig. 2 compares a model spectrum generated using the `iSpec` parameters to the LBT/PEPSI spectrum. The model spectrum is a reasonable fit to the PEPSI data. The spectroscopic parameters derived for the giant are summarized in Table 2. These estimates of the spectroscopic parameters do not consider the effects of veiling on the observed spectrum (see Section 4.4). Veiling introduces systematic uncertainties on these parameters and will lower the temperature estimate for the giant.

The spectroscopic surface gravity is consistent with that inferred from the `PHOEBE` model in Section 4.3 ($\log(g)_{\rm PHOEBE} = 1.63 \pm 0.06$). Given the spectroscopic $\log(g)$ and the radius of the giant from Section 4.3, the spectroscopic mass is $M_{\rm giant,\,spec} = 1.1 \pm 0.5\ M_\odot$, consistent with the mass of the giant derived from the `PHOEBE` model. The spectroscopic temperature is also consistent

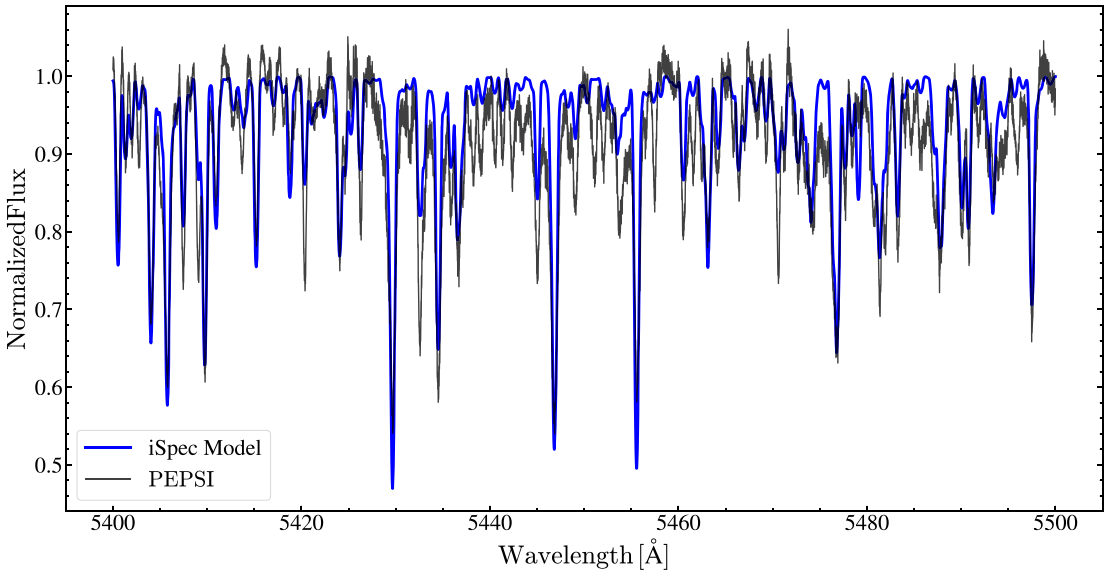

Figure 2. The LBT/PEPSI spectrum from 5400 to 5500Å (black). A model spectrum using the atmospheric parameters derived from iSpec (Table 2) is shown in blue.

Table 2. Properties of the red giant in V723 Mon (not accounting for veiling, see Section 4.4).

Parameter	FASMA	iSpec
$T_{\rm eff}$ (K)	4480 ± 50	4570 ± 60
$\log(g)$	1.7 ± 0.2	1.7 ± 0.1
[Fe/H]	-1.1 ± 0.1	-0.9 ± 0.1
[α/Fe]	—	0.7 ± 0.1
$v_{\rm mic}$ (km s^{-1})	1.64 (fixed)	0.64 ± 0.07
$v_{\rm mac}$ (km s^{-1})	5.1 (fixed)	5.7 (fixed)
$v_{\rm rot} \sin i$ (km s^{-1})*	19.1 ± 0.4	
R ($R_\odot$)	24.9 ± 0.7	
L ($L_\odot$)	173 ± 8	
M ($M_\odot$)	1.00 ± 0.07	

*Note.** $v_{\rm rot} \sin i$ varies with orbital phase

with that obtained from the SED fits. Based on the van Belle et al. (1999) temperature scale for giants, our temperature estimate is more consistent with a K0/K1 giant than the archival classification of G0 (∼6000 K) from Houk & Swift (2000). The absolute V-band magnitude ($M_V \simeq -0.3 \pm 0.1$) is consistent with a luminosity class of III (Straizys & Kuriliene 1981). From single-star evolution, the spectroscopic measurement of $\log(g)$ suggests that the giant is currently evolving along the upper red giant branch. The giant has a luminosity larger than red clump stars, suggesting that it has not yet undergone a helium flash.

We used the spectroscopic parameters in Table 2 and the luminosity constraint from the SED fit as priors to infer the physical properties of the giant using MESA Isochrones and Stellar Tracks (MIST; Choi et al. 2016; Dotter 2016). We used the `isochrones` package for the fitting (Morton 2015). We find that $M_{\rm giant,\,MIST} = 1.07 \pm 0.24\,M_\odot$ and $R_{\rm giant,\,MIST} = 24.8 \pm 4.7\,R_\odot$. The age of the giant from the MIST models is $\sim 5.4^{+5.1}_{-2.6}$ Gyr. These results are consistent with the properties of the giant derived from the spectra and the SED.

4.2 Keplerian orbit models

We fit Keplerian models both independently and jointly to the S12 and G14 radial velocities using the Monte Carlo sampler `TheJoker` (Price-Whelan et al. 2017). The results for the four fits are summarized in Table 3. We first fit each data set independently as an elliptical orbit to verify that we obtain results consistent with the published results. We then fit the joint data set using either a circular or an elliptical orbit. In the joint fits, we include an additional parameter to allow for any velocity zero-point offsets between the S12 and G14 data. For the circular orbit, we also set the argument of periastron $\omega = 0$. Since the orbit is nearly circular even for the elliptical models, we derived the epoch of maximal RV $T_{\rm RV,\,max}$ instead of the epoch of periastron. We define phases so that $T_{\rm RV,\,max}$ (BJD/TDB) corresponds to $\phi = 0.75$, the companion eclipses at $\phi = 0.5$ and the giant would be eclipsed at $\phi = 0$. After doing a first fit for the elliptical models, we did a further fit with P, K, e, γ, and $T_{\rm RV,\,max}$ fixed to their posterior values and further optimized ω using least-squares minimization.

The results of the fits are summarized in Table 3 and shown in Fig. 3. The fits to the individual data sets agree well with the published results, and the mass functions are well constrained and mutually consistent. The elliptical models all yield a small, non-zero ellipticity, consistent with G14's arguments. We do find a small velocity offset of $\Delta V = 0.58 \pm 0.14$ km s^{-1} for the elliptical model and $\Delta V = 0.84 \pm 0.21$ km s^{-1} for the circular model between the S12 and G14 data. While the velocity residuals of the fits are small compared to K ($\lesssim 1.7$ km s^{-1} versus 65 km s^{-1}), they are large compared to the measurement uncertainties. Thus, while the RV curve is clearly completely dominated by the orbital model, Fig. 3 also shows that there are significant velocity residuals for both joint fits. The circular fit is dominated by a residual of period $P_{\rm orb}/2$ and the elliptical fit is dominated by a residual of period $P_{\rm orb}/3$. Fitting an elliptical orbit with a circular orbit will show a dominant $P_{\rm orb}/2$ residual, but an elliptical orbit should not show a large $P_{\rm orb}/3$ residual. This $P_{\rm orb}/3$ residual to the fit of an elliptical orbit is likely the origin of the S12 hypothesis that the companion is an SB1 with this period. The residuals do not, however, resemble those of a Keplerian orbit. We discuss this hypothesis and the velocity residuals in Appendix A.

Binaries with evolved components [$\log(g) < 2.5$] and orbital periods shorter than ∼100 d are expected to have gone through tidal circularization and have circular orbits (e.g. Verbunt & Phinney

Table 3. Orbital elements for V723 Mon.

Parameter	S12	G14	S12 + G14	S12 + G14
$P_{\rm orb}$(d)	59.9358 ± 0.0017	59.9391 ± 0.0020	59.9394 ± 0.0014	59.9398 ± 0.0020
K (km s^{-1})	65.483 ± 0.068	65.209 ± 0.117	65.360 ± 0.081	65.150 ± 0.125
e	0.0152 ± 0.0010	0.0186 ± 0.0014	0.0158 ± 0.0012	0 (fixed)
ω (°)	89.1 ± 4.1	88.2 ± 5.8	88.4 ± 4.6	0 (fixed)
γ (km s^{-1})	1.81 ± 0.053	3.02 ± 0.07	1.95 ± 0.07	1.88 ± 0.10
$a_{\rm giant} \sin i$ (R$_\odot$)	77.567 ± 0.081	77.242 ± 0.139	77.425 ± 0.096	77.187 ± 0.148
$T_{\rm RV,\,max}$ (BJD-2450000)	4096.196 ± 0.696	4098.946 ± 0.954	4096.529 ± 0.773	4096.168 ± 0.038
RMS Residual (km s^{-1})	0.519	0.969	0.876	1.17
$f(M)$ (M$_\odot$)	1.743 ± 0.005	1.721 ± 0.009	1.734 ± 0.006	1.717 ± 0.010

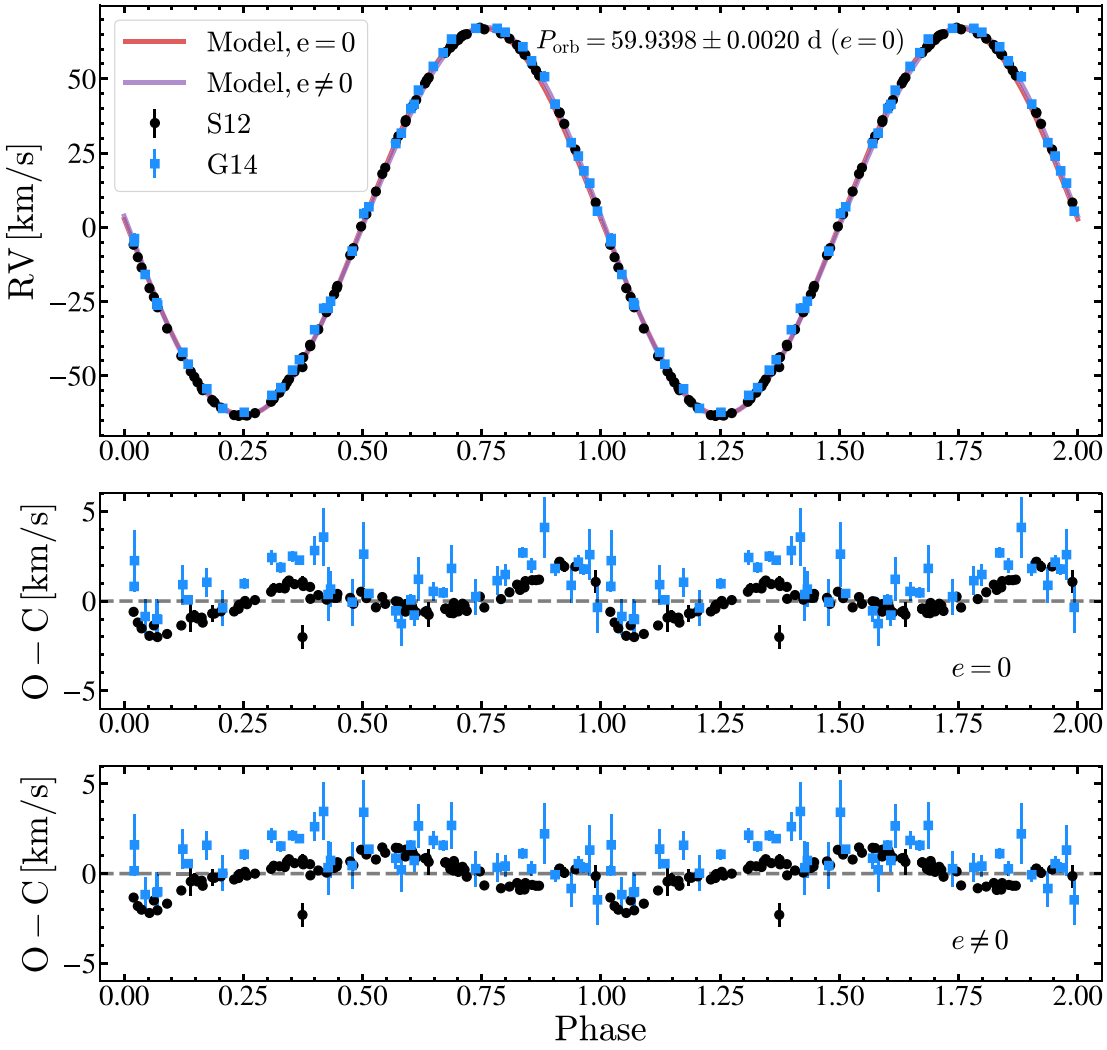

Figure 3. The observed radial velocities for V723 Mon as a function of orbital phase, defined with the epoch of maximal RV at $\phi = 0.75$ (top). The RVs from Strassmeier et al. (2012) [S12] are shown as the black circles and the RVs from Griffin (2014) [G14] are shown as the blue squares. The joint, circular (elliptical) RV fit from Table 3 is shown in red (purple). The two models closely overlap and are hard to distinguish. The residuals from both the circular and elliptical fit to the combined data are shown in the lower panels. The RV residuals are most likely a result of the ellipsoidal variability rather than the result of a triple system (see appendix A.).

1995; Price-Whelan & Goodman 2018). However, in the joint fits, the models with ellipticity are a better fit and have smaller RMS residuals than the circular models. Griffin (2014) carried out an F-test and noted that the ellipticity in their best-fitting orbit for V723 Mon was significant, and concluded that it was very likely real. While we use the circular orbit for the PHOEBE models in Section 4.3, the differences in the mass function and semimajor axis compared to the elliptical orbit are small and have no effect on our conclusions.

Independent of this issue with the origin of the RV residuals, the companion to the red giant in V723 Mon must be very massive given a mass function of 1.72−1.74 M$_\odot$. The mass function itself

is greater than the Chandrasekhar mass of $\sim$1.4 $M_\odot$, immediately ruling out a white dwarf (WD) companion. For an edge on orbit (see Section 4.3) and $M_{\rm giant} \simeq 1\,M_\odot$, the companion mass is $M_{\rm comp} \simeq 3\,M_\odot$ and the semimajor axis is $a \simeq 100\,R_\odot$. The Roche limits are approximately $R_{\rm L,\,giant} = 0.29a \simeq 30\,R_\odot$ for the giant and $R_{\rm L,\,comp} = 0.48a \simeq 49\,R_\odot$ for the companion. Based on the radius estimate from the SED fits (Section 4.1), the giant is comfortably inside its Roche lobe ($R_{\rm giant}/R_{\rm L,\,giant} \simeq 0.66$) but in the regime where we should be seeing strong ellipsoidal variability due to the tidal deformation of the giant by the gravity of the companion (e.g. Morris 1985). Any stellar companion also has to be well within its Roche lobe or it would dominate the SED because its Roche lobe is significantly larger. Hence, we can be confident that we have a detached binary whose light is dominated by a giant that should show ellipsoidal variability and might show eclipses.

4.3 PHOEBE and ELC binary models

While it has been previously claimed that V723 Mon is a contact/semidetached binary of the β-Lyrae type, we find that this is very unlikely. As we just argued, both the giant and any companion must lie well within their Roche lobes given the properties of the giant and the orbit. Additionally, the morphology of the light curve is inconsistent with those of detached and most semidetached eclipsing binaries. Here, we interpret the light curves as ellipsoidal variability and deduce limits on any eclipses of the companion for use in Section 4.5.

We fit the ASAS *V*-band, KELT R_K-band, and *TESS* *T*-band light curves (Fig. 5) using `PHOEBE 2.3` (Prša et al. 2016; Horvat et al. 2018; Conroy et al. 2020). Since the companion appears to be dark and producing no eclipses, we fix it to be a small ($R = 3 \times 10^{-6}$ $R_\odot$), cold ($T_{\rm eff} = 300$ K) blackbody, use the simplest and fastest eclipse model (`eclipse_method = only_horizon`) and do not include the effects of irradiation and reflection. We adopt the joint-circular RV solution from Table 3 (period, $e = 0$, systemic velocity, semimajor axis, and argument of periastron $\omega = 0$). We set the bolometric gravity darkening coefficient as $\beta = 0.54$, comparable to those obtained by Claret & Bloemen (2011) in the *R* band for stars with $T_{\rm eff} \sim 4600$ K, $-1 \lesssim$ [Fe/H] $\lesssim -0.5$, and $0 \lesssim \log(g) \lesssim 2$. We did not find significant differences in the final parameters when we varied β by $\pm$20 per cent in the `PHOEBE` models. A 20 per cent change in β roughly corresponds to $\Delta T_{\rm eff} \simeq 500$ K or $\Delta \log(g) \simeq 1.5$.

We initially performed trial fits to the KELT and *TESS* light curves simultaneously using the Nelder–Mead simplex optimization routine (Lagarias et al. 1998). The parameters from the trial fit were then used to initialize an MCMC sampler with 20 walkers, which was then run for 3000 iterations using the `emcee` (Foreman-Mackey et al. 2013) solver in `PHOEBE 2.3`. We fit for the binary mass ratio $q = M_{\rm giant}/M_{\rm comp}$, orbital inclination ($i$), the radius ($R_{\rm giant}$) and the effective temperature of the giant ($T_{\rm eff,\,giant}$). We marginalize over the semimajor axis of the red giant ($a_{\rm giant}\sin i$), the passband luminosities and nuisance parameters that account for underestimated errors in the KELT R_K-band and *TESS* *T*-band light curves. We adopt Gaussian priors on the effective temperature ($T_{\rm eff,\,giant} = 4440 \pm 90$ K) and the radius ($R_{\rm giant} = 22.2 \pm 0.8\,R_\odot$) based on the SED fits in Section 4.1. We adopt uniform priors of [70°, 90°] and [0, 1] for the orbital inclination and mass ratio, respectively.

The corner plot of the posterior samples for q, i, $R_{\rm giant}$, and $T_{\rm eff,\,giant}$ is shown in Fig. 4, and the results of the best-fitting `PHOEBE` model are listed in Table 4. The errors in the parameters were derived from the MCMC chains. Our model is a good fit to the KELT R_K-band and *TESS* *T*-band light curves, shown in Fig. 5. The `PHOEBE` model indicates that the orbital inclination of V723 Mon is nearly edge on ($87.0^{\circ\,+1.7^\circ}_{-1.4^\circ}$). The semimajor axis of the binary is $a_{\rm orb}\sin i = a_{\rm giant}\sin i + a_{\rm c}\sin i = 102.7 \pm 1.3$ $R_\odot$. The radius derived from the `PHOEBE` model (24.9 ± 0.7 $R_\odot$) agrees well with those obtained from the SED fits and the MIST evolutionary models in Section 4.1.

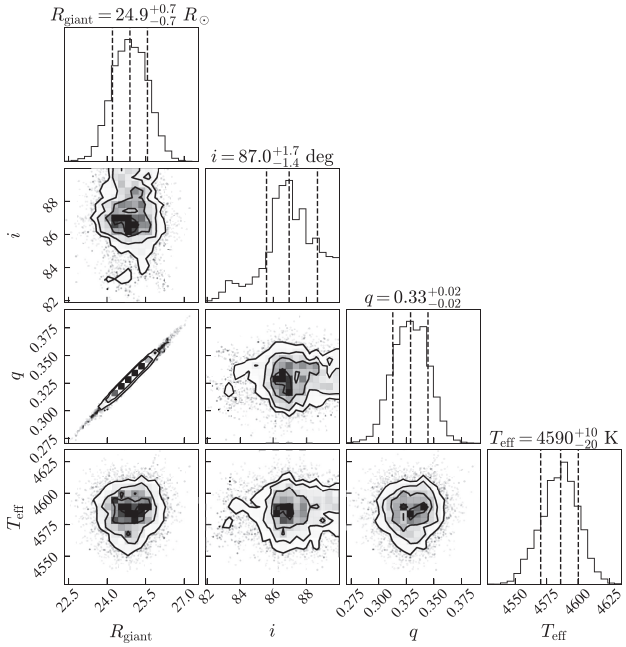

Figure 4. The corner plot for the posterior samples for q, i, $R_{\rm giant}$, and $T_{\rm eff,\,giant}$ in the best-fitting PHOEBE model to the KELT and *TESS* light curves.

Table 4. PHOEBE parameter estimates for the dark companion primary (DC) and red giant secondary (RG).

Parameter	DC	RG
$P_{\rm orb}$ (d)	59.9398 (fixed)	
ω (°)	0 (fixed)	
e	0 (fixed)	
γ (km s^{-1})	1.88 (fixed)	
$a\sin i$ ($R_\odot$)	$25.376^{+1.221}_{-1.251}$	$77.178^{+0.160}_{-0.171}$
i (°)	$87.0^{+1.7}_{-1.4}$	
$T_{\rm eff}$ (K)	300 (fixed)	4590 ± 10
R ($R_\odot$)	3×10^{-6} (fixed)	24.9 ± 0.7
q	$0.32889^{+0.01576}_{-0.01627}$	
M ($M_\odot$)	3.04 ± 0.06	1.00 ± 0.07

To verify the results of the `PHOEBE` models, we independently fit the KELT R_K-band light curve and the S12 radial velocities using the differential evolution Markov Chain optimizer (Ter Braak 2006) and the `ELC` binary modelling code (Orosz & Hauschildt 2000). The optimizer was initialized using the parameters from the Nelder–Mead simplex optimization from `PHOEBE` and the optimizer was run for 10 000 iterations using 18 chains. We fit for the mass, radius and temperature of the red giant ($M_{\rm giant}$, $R_{\rm giant}$, $T_{\rm eff,\,giant}$), the orbital inclination (i), the binary mass ratio (q), and the observed RV semi-amplitude (K) assuming uniform priors. We included priors for the temperature ($T_{\rm eff,\,giant} = 4440 \pm 90$ K), radius ($R_{\rm giant} = 22.2 \pm 0.8$ $R_\odot$), surface gravity($\log(g) = 1.7 \pm 0.2$), and $v_{\rm rot}\sin i = 19.1 \pm 1$ km s^{-1}. From the `ELC` pos-

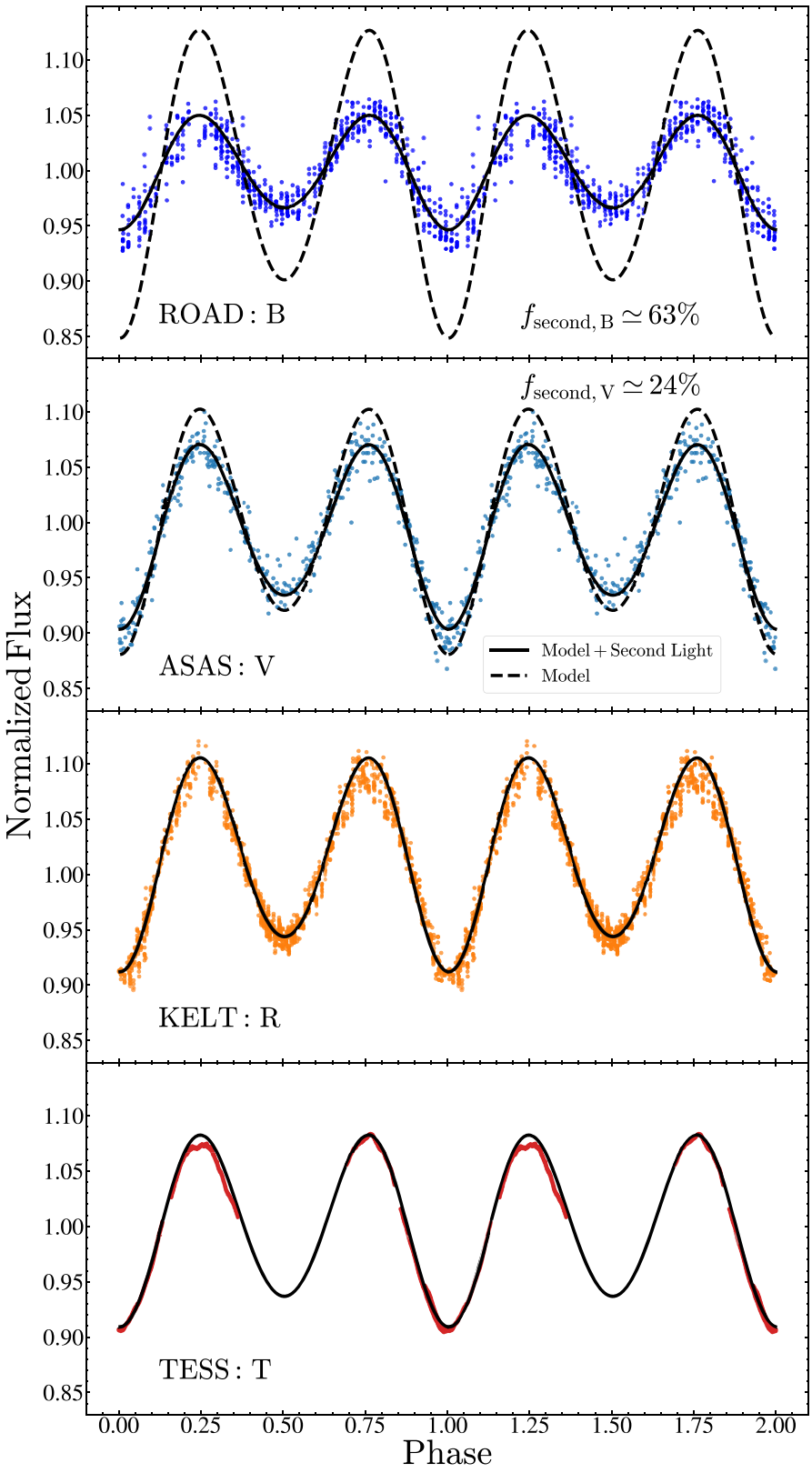

Figure 5. The normalized ROAD *B*-band, ASAS, KELT, and *TESS* light curves for V723 Mon as a function of orbital phase (defined with the epoch of maximal RV at $\phi = 0.75$). The best-fitting binary models from PHOEBE are also shown. Second light from the veiling component (see Section 4.4) is considered in the models for the *B* ($f_{\rm second,B}$∼63 per cent) and *V*-band ($f_{\rm second,V}$∼24 per cent) data.

teriors, we obtain $M_{\rm giant} = 0.99^{+0.04}_{-0.05}$ M$_\odot$, $T_{\rm eff,giant} = 4570^{+60}_{-40}$ K, $R_{\rm giant} = 24.5^{+0.4}_{-0.5}$ R$_\odot$, $i = 88.9^{\circ +0.8^\circ}_{-1.6^\circ}$, $q = 0.33443^{+0.09654}_{-0.06113}$, and $K = 65.213 \pm 0.025$ km s^{-1}. This implies that the mass of the companion is $M_{\rm comp} = 3.07^{+0.44}_{-0.28}$ M$_\odot$. The parameters obtained from ELC agree well with those obtained from PHOEBE.

With the well-constrained Keplerian model for the RVs and the PHOEBE model for the ellipsoidal variations, we are able to directly determine the masses of the two components. The mass of the companion is

$$M_{\rm comp} = \frac{f(M)(1+q)^2}{\sin^3 i} \simeq \frac{2.9\ M_\odot}{\sin^3 i} \left(\frac{f(M)}{1.7\ {\rm M}_\odot}\right) \left(\frac{1+q}{1.3}\right)^2 \quad (4)$$

and from the PHOEBE models, we find that the red giant has a mass $M_{\rm giant} \simeq 1.00 \pm 0.07\,{\rm M}_\odot$ and the companion has a mass $M_{\rm comp} \simeq 3.04 \pm 0.06\,{\rm M}_\odot$. The reported errors are purely statistical and do not consider systematic effects (veiling, etc.) in the derivation of the binary solution. However, our results in Section 4.4 indicate that the veiling in the KELT and *TESS* light curves is minimal and should not significantly bias the mass estimates. In the absence of evidence for a stellar companion in the SED, spectra, or in eclipse, perhaps the simplest explanation for the mass of the companion ($M_{\rm comp} \simeq 3.04 \pm 0.06\,{\rm M}_\odot$) is that it is a non-interacting BH in the 'mass-gap' between 3 and 5 M$_\odot$ (Özel et al. 2010; Farr et al. 2011). We discuss other scenarios in Section 5. The estimated mass of the red giant ($M_{\rm giant} \simeq 1.00 \pm 0.07\,{\rm M}_\odot$) places it towards the lower end of measured red giant masses in the APOKASC catalogue (Pinsonneault et al. 2018). Of the APOKASC sources with measured asteroseismic masses, only ∼13 per cent had masses lower than 1.0 M$_\odot$. The mass derived from the binary modelling is also very similar to the MIST estimate in Section 4.1.

Given the configuration of the binary and the large size of the giant (∼25 R$_\odot$), a companion with a radius of 1 R$_\odot$ should be eclipsed for inclination angles $i \gtrsim 76^\circ$. Fig. 6 shows the eclipses predicted for the ASAS, KELT, and *TESS* light curves for main-sequence stars with masses of 1, 1.5, and 2 M$_\odot$. Any such stars would have produced relatively easy to detect eclipses. We will focus on the KELT limits because these data have higher S/N compared to ASAS photometry, and *TESS* only observed the eclipse of the red giant and not of the companion. At the expected phase of the eclipse, the RMS of the KELT data relative to the eclipse-free ellipsoidal (ELL) model is only 0.84 per cent for phases from 0.46 to 0.54. If we bin the data 0.01 in phase, the RMS of the binned data is only 0.38 per cent. We will adopt a very conservative KELT band eclipse limit of 1 per cent. Similarly, based on the *Swift*, ASAS, and ROAD light curves, we will adopt eclipse limits of 10 per cent, 3 per cent, and 2 per cent for the *UVM2*, *B* and *V* bands, respectively. The *Swift UVM2* light curve is shown in Fig. 7. The *UVM2* light curve appears somewhat variable, with one larger outlier on UT 2020-11-13 ($\phi \simeq 0.35$). However, we do not see any evidence for an eclipse at the (conservative) level of ∼10 per cent at the expected phases $0.46 \lesssim \phi \lesssim 0.54$. While the *TESS* light curve does not cover the eclipse of the companion at $\phi = 0.5$, it does cover the eclipse of the giant at $\phi = 0$. For this eclipse, we estimate a conservative limit on the *TESS* band eclipse depth of ∼0.3 per cent.

4.4 Veiling

After the KELT R_K-band and *TESS T*-band light curves were jointly fit, we compared the resulting model *V*-band light curve to the ASAS observations, and found that the observed *V*-band variability amplitude was smaller than predicted by our model. Lower amplitudes at (usually) bluer wavelengths are generally attributed to an additional source of diluting ('second') light. For X-ray binaries, it is also known as 'disc veiling' due to additional light from accretion (e.g. Hynes, Robinson & Bitner 2005; Wu et al. 2015). The amount of additional flux is usually characterized either by the ratio r of the veiling flux to the stellar flux or the veiling flux as a fraction of the total flux $f = r/(1+r)$. Interacting X-ray binaries are frequently observed to have veiling factors upwards of $f_{\rm disk}$∼50 per cent, corresponding to $r \sim 1$ (see e.g. Wu et al. 2015).

We fixed the system parameters to those from the joint fit to the KELT + *TESS* light curves and fit for additional flux (second light) in the *V* band. The fit to the ASAS *V*-band light curve is consistent with an additional *V*-band flux (F_2) amounting to $f_{\rm second,V} = F_2/(F_2 + F_{\rm giant}) = 24 \pm 2$ per cent. Fig. 5 shows the PHOEBE model fit for the *V*-band after accounting for this additional flux. The redder ROAD R_c and I_c light curves agree well with the PHOEBE model without additional flux. The ROAD observations also agree with the PHOEBE model for the *V* band with the additional flux ($f_{\rm second,V} = 24 \pm 2$ per cent) added. The discrepancy between the *B*-band light curve and a model without extra flux is even larger than for the *V* band. Fitting the *B*-band data requires a larger second light contribution of $f_{\rm second,B} = 63 \pm 2$ per cent. The colour of the extra light $B - V = -0.2 \pm 0.1$ is very blue even before applying any extinction corrections. This corresponds to stars with $T_{\rm eff}$ ranging from ∼13 000 to ∼30 000 K (Papaj, Krelowski & Wegner 1993). However, no hot star could have a rapidly rising SED from *V* to *B* and then drop rapidly from *B* to the *UVM2*-band. Stellar SEDs are intrinsically broader in wavelength, like the model in Fig. 1. Additionally, stars with these temperatures are easily ruled out by constraints from the SED and eclipses (see Section 4.5).

Veiling also affects the spectrum of the star (line veiling) by reducing the observed depths of stellar absorption features. This is a well-known problem in interacting X-ray binaries (see e.g. Casares et al. 1993) and T-Tauri systems (Gahm et al. 2008). Veiling in spectroscopic observations is characterized through the fractional veiling

$$r(\lambda) = \frac{V(\lambda)}{S(\lambda)}, \quad (5)$$

where $V(\lambda)$ is the veiling spectrum and $S(\lambda)$ is the uncontaminated spectrum of the star (Casares et al. 1993). The ratio $r(\lambda)$ is related to the second light (F_2) as

$$F_2 = r(\lambda) F_{\rm giant}, \quad (6)$$

where $F_{\rm giant}$ is the flux from the giant. The observed spectrum of the star is a function of the veiling factor $F_{\rm veil}(\lambda) = 1 + r(\lambda)$

$$r(\lambda) = A(\lambda) S(\lambda) F_{\rm veil}(\lambda), \quad (7)$$

where $A(\lambda)$ is a normalization factor. The monochromatic veiling factor

$$F_{\rm veil} = \frac{{\rm EW_s}}{{\rm EW_{obs}}} \quad (8)$$

is the ratio of the observed EWs to those predicted from the standard/synthetic spectrum.

We calculated the monochromatic veiling factors for various Ca I and Fe I absorption lines in the SES spectra and the red side of the PEPSI spectrum ($\lambda > 500$ nm). For the Ca lines, we assumed an abundance of $[{\rm Ca/H}] = 0.02 \pm 0.02$ derived from the PEPSI spectrum. We generated a synthetic iSpec/SPECTRUM (Gray & Corbally 1994) spectrum for the red giant using the atmospheric parameters in Table 2. Since the $R \approx 220\,000$ PEPSI spectrum has

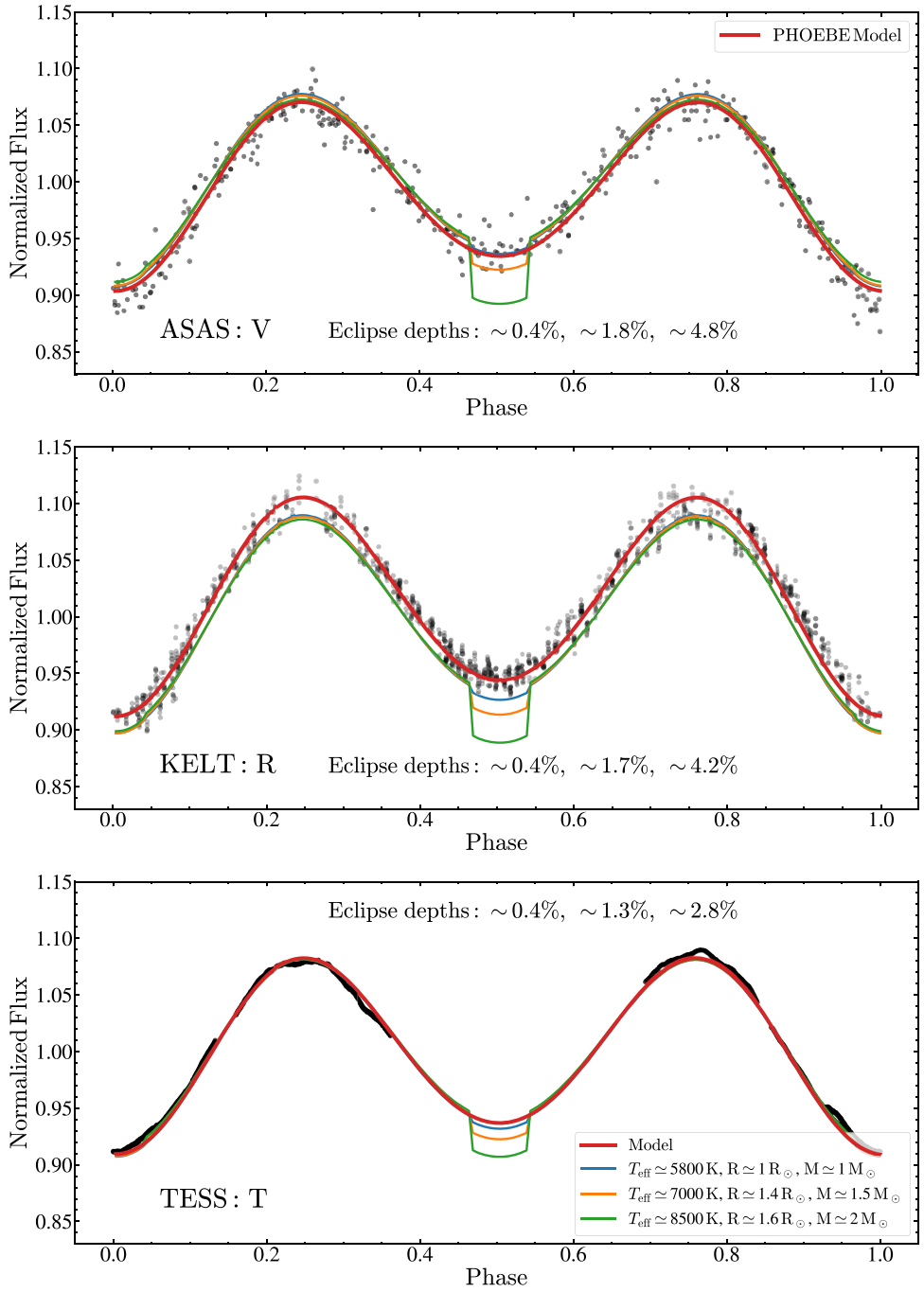

Figure 6. The observed ASAS, KELT, and *TESS* light curves compared to various eclipsing models with main-sequence companions to the red giant. The ellipsoidal model is shown in red. The depths of the eclipses at $\phi = 0.5$ compared to the non-eclipsing ellipsoidal model is also shown. Eclipse constraints rule out single and binary stellar companions with $M_{\rm single} > 0.80$ M$_\odot$ and $M_{\rm binary} > 1.51$ M$_\odot$ (see Section 4.5).

lower S/N at blue wavelengths, we use the mean veiling factors in the SES spectra for the absorption lines blue-ward of 500 nm. We use the standard deviations of the estimates from the individual SES spectra to estimate the uncertainties. For the redder lines at >500 nm, we use the veiling factors derived from the PEPSI spectrum at $\phi \simeq 0.63$ and assign errors of ± 0.10 in $r(\lambda)$. This method can have large systematic uncertainties (see Casares et al. 1993), but it provides a way to independently test the estimates from the dependence of the ellipsoidal variability amplitudes on wavelength.

Fig. 8 shows that the fractional veiling and second light as a function of wavelength $r(\lambda)$ rises steeply towards bluer wavelengths, with a power-law (λ^α) index of $\alpha \simeq -5.0 \pm 1.5$, steeper than that expected from the Rayleigh–Jeans law ($\alpha = -4$). These results also indicate minimal contamination in the KELT R_K and *TESS T* filters that are used for our primary fits to the ellipsoidal variations. As a precaution, we ran PHOEBE models adding 10–20 per cent extra flux in the KELT R_K band, and found that the masses of the red giant and dark companion are comparable to those obtained without

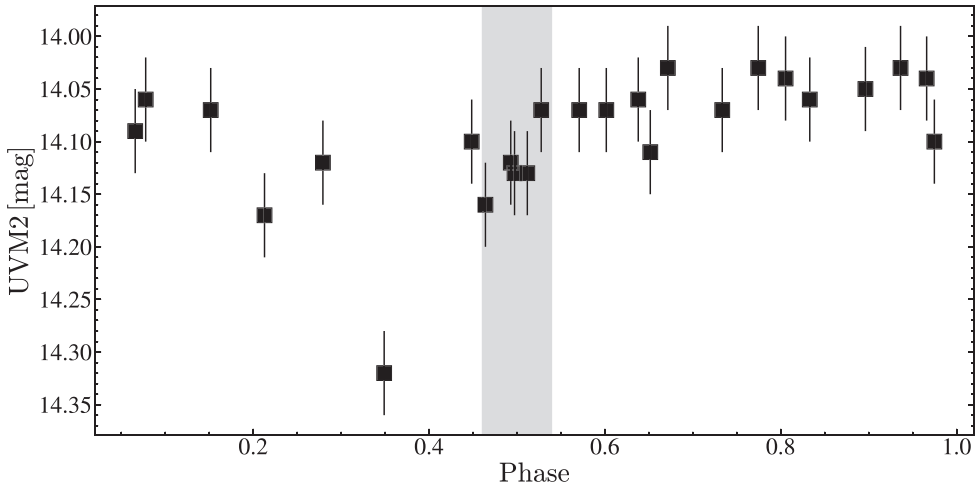

Figure 7. The *Swift* UVM2 light curve. The expected eclipse duration (∼5 d) of the companion is highlighted in red.

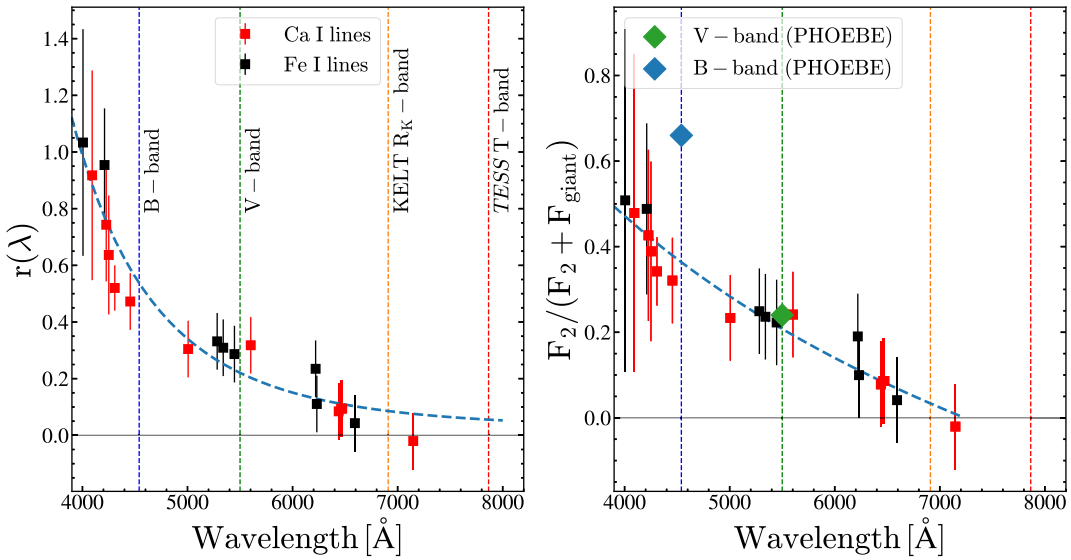

Figure 8. The fractional veiling $r(\lambda$; Equation 5) [left] and second light (Equation 6) [right] calculated using Ca I and Fe I absorption lines as a function of wavelength. The fractional second light in the *BV*-bands as calculated from PHOEBE are shown as the filled diamonds. Power-law fits are shown as the blue-dashed lines. The effective wavelengths of the BVR_KT bands are shown as the dashed lines.

considering veiling given the error estimates. The fractional second light in the V band from the PHOEBE fits is comparable to that derived from the line veiling estimates. The PHOEBE estimate of the second light in the B band is somewhat larger than that seen in the line veiling, however, both estimates indicate a large contribution to the B-band flux. Based on the lack of eclipses in the light curves (see Section 4.5), we can also infer that this emission component has to be diffuse.

Since the second light has a non-negligible contribution to the total SED of V723 Mon for $\lambda \lesssim 600$ nm, the inferred properties of the star from Section 4.1 can also be affected. We refit the SED of the giant after removing the estimated veiling component to obtain $T_{\rm eff,\,giant} \simeq 4150 \pm 100$ K, $L_{\rm giant} = 153 \pm 9\ L_\odot$, $R_{\rm giant} \simeq 24.0 \pm 0.9\ {\rm R}_\odot$ and $E(B-V) \simeq 0.069 \pm 0.044$ (Fig. 9). The veiling component contributes ∼12 per cent of the total SED flux, with most of the flux in the bluer wavelengths. We perform iSpec fits to the PEPSI spectrum after truncating it to the redder wavelengths at $\lambda > 600$ nm that are minimally affected by veiling. We obtain $T_{\rm eff} = 4350 \pm 50$ K, $\log(g) = 2.0 \pm 0.1$, [Fe/H] $= -0.7 \pm 0.1$, $[\alpha/{\rm Fe}] = 0.3 \pm 0.1$, and $v_{\rm micro} = 0.8 \pm 0.1\ {\rm km\,s^{-1}}$. From the parameters listed in Table 2, these differ by $\Delta T_{\rm eff,\,giant} \simeq 220$ K, $\Delta\log(g) \simeq 0.3$, and Δ[Fe/H] $\simeq 0.3$. In contrast, the parameters derived from the PHOEBE fits (Table 4) do not change significantly if we change $T_{\rm eff,\,giant}$. Because the models of the veiled SED are driven to larger, cooler stars, models forcing the star to be more compact are even more disfavored than in the unveiled models. The best model of the veiled SED has $\chi^2 = 14.2$, rising to 33.9 for $R_{\rm giant} = 20\ {\rm R}_\odot$ and to 64.0 for $R_{\rm giant} = 18\ {\rm R}_\odot$.

The origin of this veiling component remains unclear, although it is clearly non-stellar in nature. However, the morphology of the veiling component is broadly compatible with the spectra of advection dominated accretion flows (ADAF). ADAF spectra can be described by contributions due to synchrotron emission, Compton scattering and Bremsstrahlung radiation (Quataert & Narayan 1999). The most luminous feature in the ADAF models come from the synchrotron peak and for stellar mass BHs, this peak falls in the

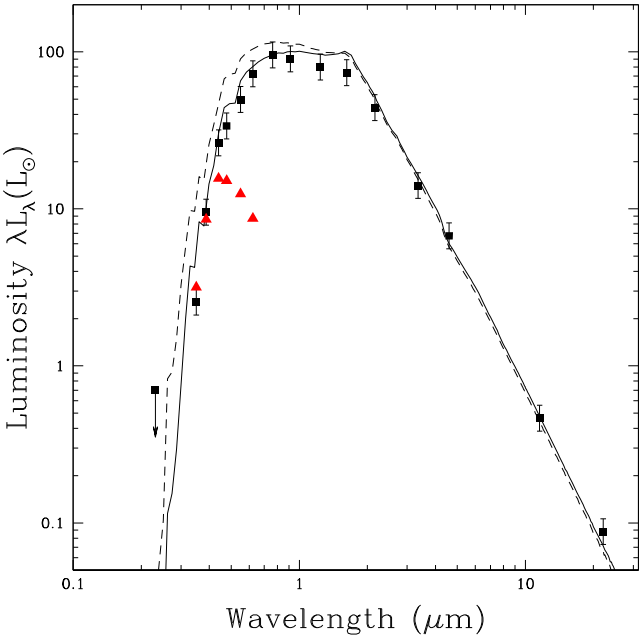

Figure 9. The best-fitting SED model for V723 Mon after correcting for the veiling component (the red triangles). The uncorrected SED from Fig. 1 is also shown (dashed line). Note that the SED of the veiling component is very different from the SEDs of stars, as can be seen by comparing to Fig. 1.

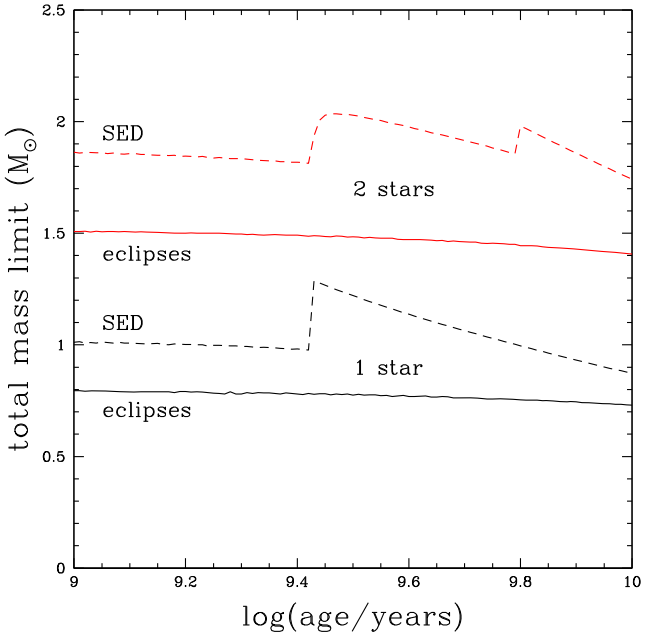

Figure 10. Limits on the mass of a companion that is comprised of either one (black) or two (red) luminous stars based on either the lack of KELT eclipses (solid) or the SED (dashed) as a function of the age of the stars. From these limits, the maximum allowed mass for a single star is 1.29 $M_\odot$ (SED) and 0.80 $M_\odot$ (eclipses). For two stars, the maximum allowed mass is 1.98 $M_\odot$ (SED) and 1.51 $M_\odot$ (eclipses).

optical wavelengths (Quataert & Narayan 1999). In their ADAF models for quiescent BH binaries ($M_{\rm BH} = 6\,M_\odot$) with low accretion rates ($\log(\dot{M}/\dot{M}_{\rm edd}) \sim -4$), Esin, McClintock & Narayan (1997) show that the SED peaks at optical wavelengths and rapidly decays at both longer and shorter wavelengths. For V723 Mon, detailed ADAF models are necessary to determine whether the veiling component is related to accretion flows around the dark companion, but such analysis is beyond the scope of this paper.

4.5 Limits on luminous stellar companions

We can constrain the presence of luminous companions using either the SED or the absence of eclipses. The limits using only the SED will be weaker than those using the eclipses, but are also independent of any knowledge of the inclination. For the SED constraints, we require that the companion contributes less than 100 per cent, 60 per cent, and 20 per cent of the light in the *UVM2*, *B,* and *V* bands, respectively. The *B*- and *V*-band limits correspond to the estimated veiling source from Section 4.4 and are conservative since the SED of the veiling light appears to be inconsistent with a star, and the *UVM2* band limit is simply the total observed flux because we lack any constraint on the amount of veiling for this band. For the eclipse constraints, we require that the companion contributes less than 10 per cent, 3 per cent, 2 per cent, and 1 per cent in the *UVM2*, *B*, *V,* and *R* bands based on the eclipse models in Section 4.3. While we did not use the *UVM2* band in the SED fits because the SED models cannot account for any possible chromospheric emission from the rapidly rotating giant, there is no issue with using them to obtain these limits.

To provide models for the relationships between luminosity, temperature and mass, we sampled stars from [Fe/H] = −1 PARSEC (Bressan et al. 2012) isochrones with ages from 1 to 10 Gyr, and we logarithmically interpolated along each isochrone to sample more densely in mass. We considered models in which the companion is either a single star or two stars. In the latter case, we considered all combinations of two stars on the same isochrone. The age of the stars is the principal variable leading to changes in the mass limits, but the differences are not large. Two star models will generically allow higher limiting masses for two reasons. First, since luminosity is a steeply rising function of mass, dividing a single star into two lower mass stars of the same total mass leads to a lower total luminosity. Secondly, the two lower mass stars are also cooler on the main sequence, so they produce less blue light per unit luminosity than the single star, which also allows the total mass be larger for the same constraints on the bluer fluxes.

We start with the weaker but inclination independent limits from the SED, where Fig. 10 shows the mass limits as a function of stellar age. For a single star, the maximum allowed mass is 1.29 $M_\odot$ ($\log(\text{age}) = 9.49$, $L = 15.5\ L_\odot$, $T = 5430$ K), and it occurs where the star is just starting to evolve off the main sequence because the initial drop in temperature weakens the constraints more than the rise in luminosity (see Fig. 1). There are two maximum masses for models with two stars. The lower age peak corresponds to pairing a slightly evolved star with a lower mass main-sequence star. The total mass of 1.98 $M_\odot$ comes from combining a 1.25 $M_\odot$ ($L = 12.0\ L_\odot$, $T = 5510$ K) star with a 0.77 $M_\odot$ ($L = 0.5\ L_\odot$, $T = 5900$ K) star at $\log(\text{age}) = 9.45$. The higher age peak comes from combining two stars of the same mass. The total mass is again 1.98 $M_\odot$ and the two components each have $M = 0.99\ M_\odot$ ($\log(\text{age}) = 9.80$, $L = 8.5\ L_\odot$, $T = 5430$ K). Fig. 1 shows the SEDs of these three models as compared to that of the giant, and they are nearly identical.

For the BH candidates LB1 and HR 6819, the stellar companions seemed 'dark' because they were hot. This cannot be the case here because of the tight *UVM2* luminosity limit of $\lambda L_\lambda \approx 2\ L_\odot$ (after correcting for extinction). Models normalized by this luminosity only have total luminosities of 4, 5, and 75 $L_\odot$, for temperatures of 10^4, 3×10^4, and 10^5 K, respectively, much too low for a massive

He star companion. For example, a Helium star with $T \sim 10^5$ K will have $M \sim 8\,M_\odot$ and $L \sim 90\,000\,L_\odot$ (Gräfener, Owocki & Vink 2012). For any hot companion with a luminosity approaching that of the giant, we would also expect to see the effects of irradiation of the giant on its light curve and phase dependent spectra, but no such perturbations are seen.

Given the size of the orbit and the size of the giant, companions with radii similar to those allowed by the SED will be eclipsed provided the inclination angle is $i \gtrsim 76^\circ$. While the systematic uncertainties on the estimated inclination of $87.0^{\circ\,+1.7^\circ}_{-1.4^\circ}$ may be moderately larger, the light-curve shapes at inclinations anywhere approaching this upper limit for seeing eclipses are grossly incompatible with the observations. Fig. 10 also shows the limits on masses using the flux limits on the companion required to avoid visible eclipses, and they are stronger than those from the SED as expected. The biggest change is that they eliminate the 'bumps' associated with stars starting to move off the main sequence because they more directly constrain the size of any companion. The improvements are otherwise modest because the (blue) luminosities are such strong functions of mass that moderate changes in the limits on the luminosity produce very modest changes in the limits on the mass. The single star limit is now $0.80\,M_\odot$ and the two star limit is $1.51\,M_\odot$ where the two star limit is always weakest for the stars being twins. These limits are smaller than the binary mass function for this system (see Section 4.2).

4.6 Balmer H α and H β emission

We find that the Balmer H α and Hβ lines appear to significantly vary with phase (Fig. 11) and this is unusual for a red giant. Given our phase convention, the dark companion will be eclipsed by the giant at $\phi = 0.50$ with an eclipse duration of $t_{\rm ecl} \simeq 5$ d. If a companion is responsible for Balmer emission, the subtraction of a template spectrum near phase $\phi = 0.50$ should isolate its contribution. To explore this, we subtracted the SES spectrum of the red giant near $\phi \simeq 0.5$ from the remaining spectra with $S/N > 30$.

Fig. 11 shows the changes in the H α, H β, Ca I λ6439, and Ca I λ6463 lines with orbital phase. The left-hand panel shows the continuum normalized spectra, the middle panel shows the EWs, and the right-hand panel shows the residuals relative to the spectrum observed when the companion should be in eclipse. A first point to note is that all four lines show a phase-dependent change in EW that mirrors the ellipsoidal variability – this effect is well known (e.g. Neilsen, Steeghs & Vrtilek 2008) and further confirms the origin of the variability (Section 4.3). The Balmer absorption lines appear to be blue shifted by $\sim$12 km s^{-1} (Fig. 12). This is also seen in the spectra close to conjunction at $\phi = 0.5$ (Fig. 11). However, we do not see a similar shift in the other photospheric lines. The second point to note is that while photospheric absorption lines such as Ca I λ6439 and Ca I λ6463 lines are cleanly subtracted, the H α and H β emission clearly varies with orbital phase. We do not see the Ca II H&K lines in emission, so the changes in the Balmer lines are unlikely to be caused by chromospheric activity. The Balmer emission could be caused by mass loss from the red giant through a stellar wind.

The typical Gaussian full width at half-maximum of the H α and H β emission profiles is $\sim$290 km s^{-1}. The median EW of the residual H α and H β lines is EW(H α) = 1.79 $\pm$ 0.02 and EW(H β) = 2.72 $\pm$ 0.02, respectively. We can convert the H α EW to the flux at the stellar surface using $F_{\rm H\alpha} = F_{\rm c}$ EW(H α) (see e.g. Soderblom et al. 1993; González Hernández & Casares 2010). $F_{\rm c}$ is the continuum flux that we derive using Hall (1996) as $\log(F_{\rm c}) = 7.538 - 1.081(B - V)_0$. For V723 Mon, we find $(B - V)_0 = 0.85 \pm 0.06$ mag, using the APASS DR10 photometry and the $E(B - V)$ from the SED fits. We obtain $\log(F_{\rm c}) = 6.61 \pm 0.06$ and $F_{\rm H\alpha} = 7.3 \pm 1.0$ ergs cm^{-2} s^{-1}. Normalizing the H α flux to the bolometric flux (i.e. $R_{\rm H\alpha} = F_{\rm H\alpha}/\sigma T^4$), we obtain $\log(R_{\rm H\alpha}) = -3.53 \pm 0.06$. $\log(R_{\rm H\alpha})$ is usually compared to the Rossby number $R_0 = P_{\rm rot}/\tau_c \sim 2.84$, where $\tau_c \approx 21.1$ d based on Noyes et al. (1984) and assuming that the giant's rotation is fully synchronized with the orbital period. At this value of R_0, V723 Mon has a value of $\log(R_{\rm H\alpha})$ higher than any of the chromospherically active single stars from López-Santiago et al. (2010; see fig. 5 in González Hernández & Casares 2010). This also indicates that the observed H α emission is not just from chromospheric activity.

Another argument against chromospheric activity is that the changes in the Balmer lines with phase are coherent over the $\sim$3.5 yr spanned by the SES data. If the Balmer emission was dominated by chromospheric activity, we would expect the structure to change with time as the spot patterns evolve. At RV quadrature ($\phi \simeq 0.25$ and $\phi \simeq 0.75$), the emission profiles of the Balmer lines resemble P-Cygni profiles with both absorption and emission components. This is illustrated in Fig. 13. In comparison, the Ca I λ6439 line is cleanly subtracted and does not show a similar correlation with the phase of the binary orbit. P Cygni profiles tend to be associated with mass outflow and stellar winds. At RV minimum ($\phi \simeq 0.25$), the absorption component in the Balmer lines is red shifted whereas at RV maximum ($\phi \simeq 0.75$), the absorption is blue shifted. In the rest frame of the giant, the peak of the H α emission component is relatively stationary at ~ -35 km s^{-1}. The median separation between the absorption and emission components in H α is $\Delta V \sim$115 km s^{-1}, however, this appears to vary with orbital phase. The separation is largest for $0 \leq \phi \leq 0.25$, with $\Delta V \sim$148 km s^{-1}, and drops thereafter. The smallest separation between the two components is seen at phases $0.5 \leq \phi \leq 0.75$, with $\Delta V \sim$104 km s^{-1}. Much like with the SES spectra, we also see clear variability in the Hα line profiles in the HIRES spectra (Fig. 14), and the asymmetry in the HIRES line profiles also reverses after $\phi = 0.5$.

Remarkably, near conjunction ($\phi \simeq 0.5$) there is very little Balmer emission (Fig. 13). Both the Balmer and photospheric lines are modulated with the ellipsoidal variations (Fig. 11), however, near $\phi \simeq 0.5$, the EW of the Balmer lines increases abruptly, signalling a dramatic drop in Balmer emission. A similar EW increase is not seen in the photospheric lines. This feature is coincident with the eclipse of the unseen companion by the red giant and has the expected duration. The MODS spectra were taken around the eclipse of the dark companion by the red giant at $\phi \simeq 0.5$ and the depths of the MODS Balmer H α and H β absorption features also deepen during the eclipse.

While we have clear evidence to show the presence of Balmer emission that is correlated with the orbital motion of the putative BH (Section 4.6), the exact origin of the Balmer emission is unclear. One explanation for this additional luminosity and the variability in the Balmer lines is from an accretion flow. Alternative explanations for the Balmer emission can come from a stellar wind and/or mass outflow at the inner Lagrangian point (L_1). At $\phi = 0$, the inner Lagrangian point is directed toward the observer. This also coincides with the deeper minimum in the light curve because the surface gravity and brightness is smallest at L_1 (Beech 1985). Conversely, at $\phi = 0.5$, L_1 points away from the observer. It is possible that the Balmer emission is associated with the photoionization of matter streaming through the inner Lagrangian point. The nearly constant velocity offset of the emission peak from the secondary is also consistent with this interpretation. However, this scenario requires a source of photoionization. The NS binary 1FGL J1417.7−4402

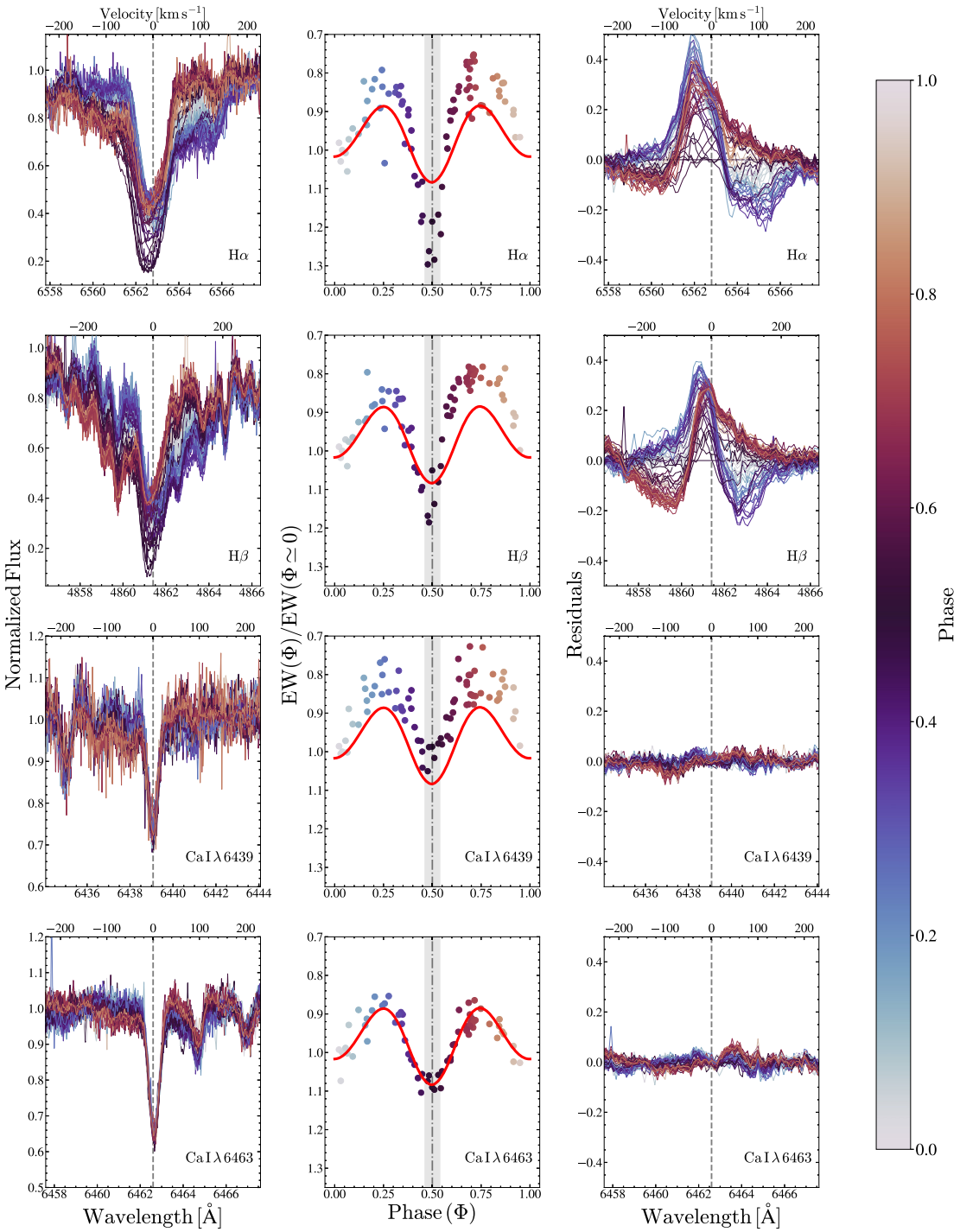

Figure 11. SES line profiles for the Balmer Hα, Hβ, Ca Iλ6439, and Ca Iλ6463 lines as a function of orbital phase (left). The middle column shows the equivalent width normalized to $\phi \simeq 0$ as a function of phase. A simple sinusoidal model (red) is fit to the variations in the Ca Iλ6463 line to illustrate the variations in the equivalent width due to ellipsoidal variations. The grey-shaded region illustrates the duration of the eclipse ($\sim$5 d). The right column shows the residuals of the line profiles after a template for the giant is subtracted.

also has a persistent Hα line with a complex morphology (Strader et al. 2015; Swihart et al. 2018). Instead of an accretion disc, the authors attributed this behaviour to the interaction between the magnetically driven wind from the secondary and the pulsar wind. Balmer photons originating from an interbinary shock or the wind from the secondary will have a velocity offset from the secondary. This is also seen in V723 Mon. However, the Hα line in 1FGL J1417.7−4402 is significantly different from what is observed in V723 Mon as it has a double-peaked emission profile that is observed directly in the spectra without the need for template subtraction. Swihart et al. (2018) also did not find independent evidence of a disc through their light curves, whereas we see clear

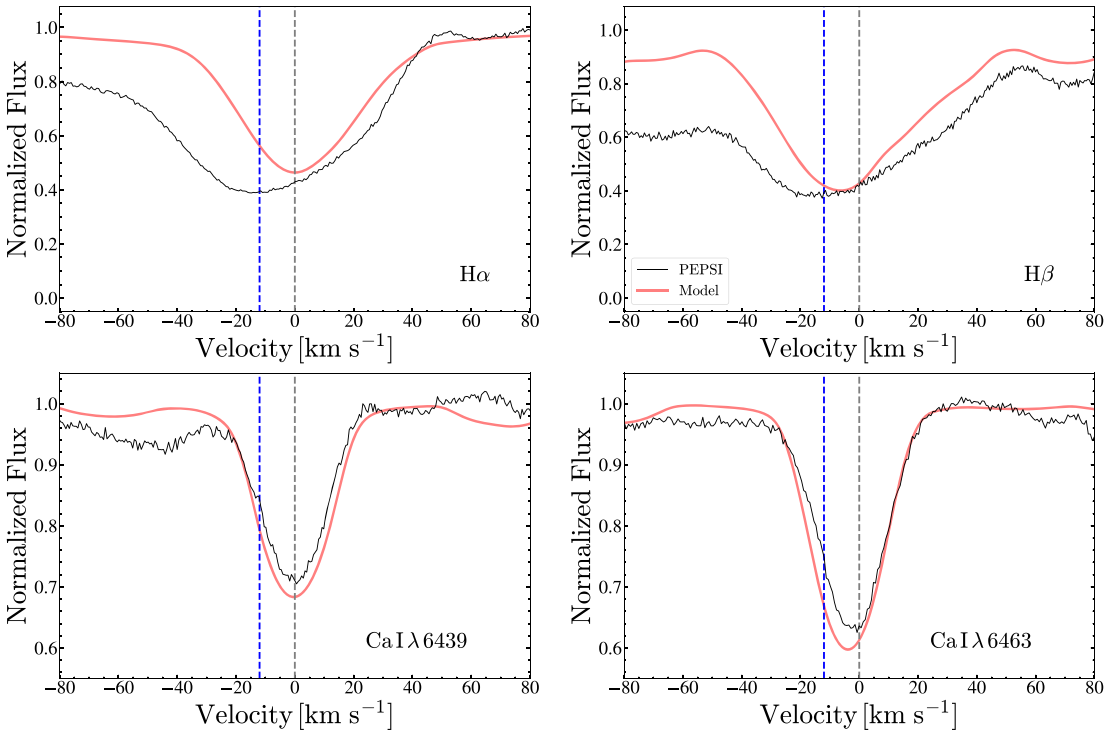

Figure 12. LBT/PEPSI line profiles for the Balmer Hα, Hβ, Ca I λ6439, and Ca I λ6463 lines (black). A model spectrum using the atmospheric parameters derived in Section 4.1 is shown in red. The blue lines show the velocity offset of the Balmer absorption lines ($\sim$12 km s^{-1}) from the rest frame of the giant.

evidence of second light in the *B*- and *V*-band light curves for V723 Mon.

In summary, we see evidence of broad Balmer emission in the spectra. The Balmer line profiles prior to when the unseen companion is eclipsed by the giant ($0 \leq \phi \lesssim 0.46$) resemble P-Cygni profiles, with a blue shifted emission component and a red shifted absorption component in the rest frame of the giant. When the unseen companion is behind the giant at $\phi \simeq 0.5$, both the Balmer components disappear and the Balmer absorption features from the giant become deeper. When the unseen companion re-emerges after the eclipse at phases $0.54 \lesssim \phi \leq 1$, we see a clear change in the P-Cygni-like line profile, with both the absorption and emission components blue shifted. However, the absorption component is blue shifted more than the emission and the P-Cygni profile is reversed. We also see significant changes in the Balmer line depths at $\phi = 0.5$ when the companion is eclipsed. The exact origin of the Balmer emission, be it from an accretion disc around the BH, a stellar wind, mass flow into an inner Lagrange point in the binary, or a combination of these, remains unclear.

4.7 X-ray detection

In the individual *Swift* XRT exposures, we only detected a source above the background in the exposures taken on 2020-11-05 ($\phi \simeq 0.2$), 2021-01-21 ($\phi \simeq 0.5$), and 2021-02-20 ($\phi \simeq 0.0$) with 4.2 ± 2.2, 6.8 ± 2.9, and 3.7 ± 2.2 background-subtracted counts in the 0.3–2.0 keV energy range, respectively. In the merged *Swift* XRT data, we detect a source with 18.5 ± 4.9 background-subtracted counts in the 0.3–2.0 keV energy range, corresponding to an aperture corrected count rate of $(1.4 \pm 0.4) \times 10^{-3}$ counts s^{-1}. Assuming that $E(B-V) \simeq 0.086$ from Section 4.1, and using the relationship between reddening and atomic hydrogen column density from Liszt (2014), the Galactic column density towards V723 Mon is $N_{\rm H,V723} \simeq 7.1 \times 10^{20}$ cm^{-2}. This is considerably smaller than the total column density in the line of sight towards V723 Mon ($N_{\rm H,LOS} = 3.42 \times 10^{21}$ cm^{-2}). Assuming an absorbed power-law with a photon index of 2 and the Galactic column density estimate $N_{\rm H,\,V723}$, the *Swift* XRT count rate corresponds to an absorbed flux of $(3.0 \pm 0.8) \times 10^{-14}$ ergs cm^{-2} s^{-1} or an unabsorbed flux of $(4.1 \pm 1.0) \times 10^{-14}$ ergs cm^{-2} s^{-1} in the 0.3–2.0 keV energy range. At the *Gaia* EDR3 distance, we obtain absorbed and unabsorbed X-ray luminosities of $(7.6 \pm 2.0) \times 10^{29}$ and $(1.0 \pm 0.3) \times 10^{30}$ ergs s^{-1}, respectively. If we use a 0.3–10.0 keV energy range, we obtain a similar number of counts as there is very little emission >2.0 keV.[13] We also derive a limit on the hardness ratio[14] of -0.21 that indicates a relatively soft emission spectrum that is consistent with the lack of hard X-ray emission above 2.0 keV. After grouping the XRT observations by orbital phase, we calculate the out-of-eclipse and in-eclipse absorbed X-ray luminosities as $(6.1 \pm 2.2) \times 10^{29}$ and $(9.3 \pm 3.1) \times 10^{29}$ ergs s^{-1} respectively. The out-of-eclipse and in-eclipse X-ray luminosities are consistent given the measurement uncertainties.

In the *XMM–Newton* observation, V723 Mon is not detected above the background, so we derive an upper-limit on $L_{\rm X}$. We find a 3σ upper-limit count rate of 4.17×10^{-2} counts s^{-1} in the 0.5–8.0 keV band within a 60 arcsec aperture (consistent with the off-axis PSF at the source position). Assuming an absorbed power-law with a photon index of 2 and the Galactic column density of $N_{\rm H,\,V723}$, we

[13] We derive a 3σ upperlimit of 1.2×10^{-4} counts s^{-1} to the 2.0–10.0 keV count rate, which corresponds to an absorbed flux of 1.4×10^{-14} ergs s^{-1} and a luminosity of 3.6×10^{29} ergs s^{-1}.

[14] Here, the hardness ratio is defined as $HR = (H-S)/(H+S)$, where H is the number of counts in the 2.0–10.0 keV energy range and S is the number of counts in the 0.3–2.0 keV energy range.

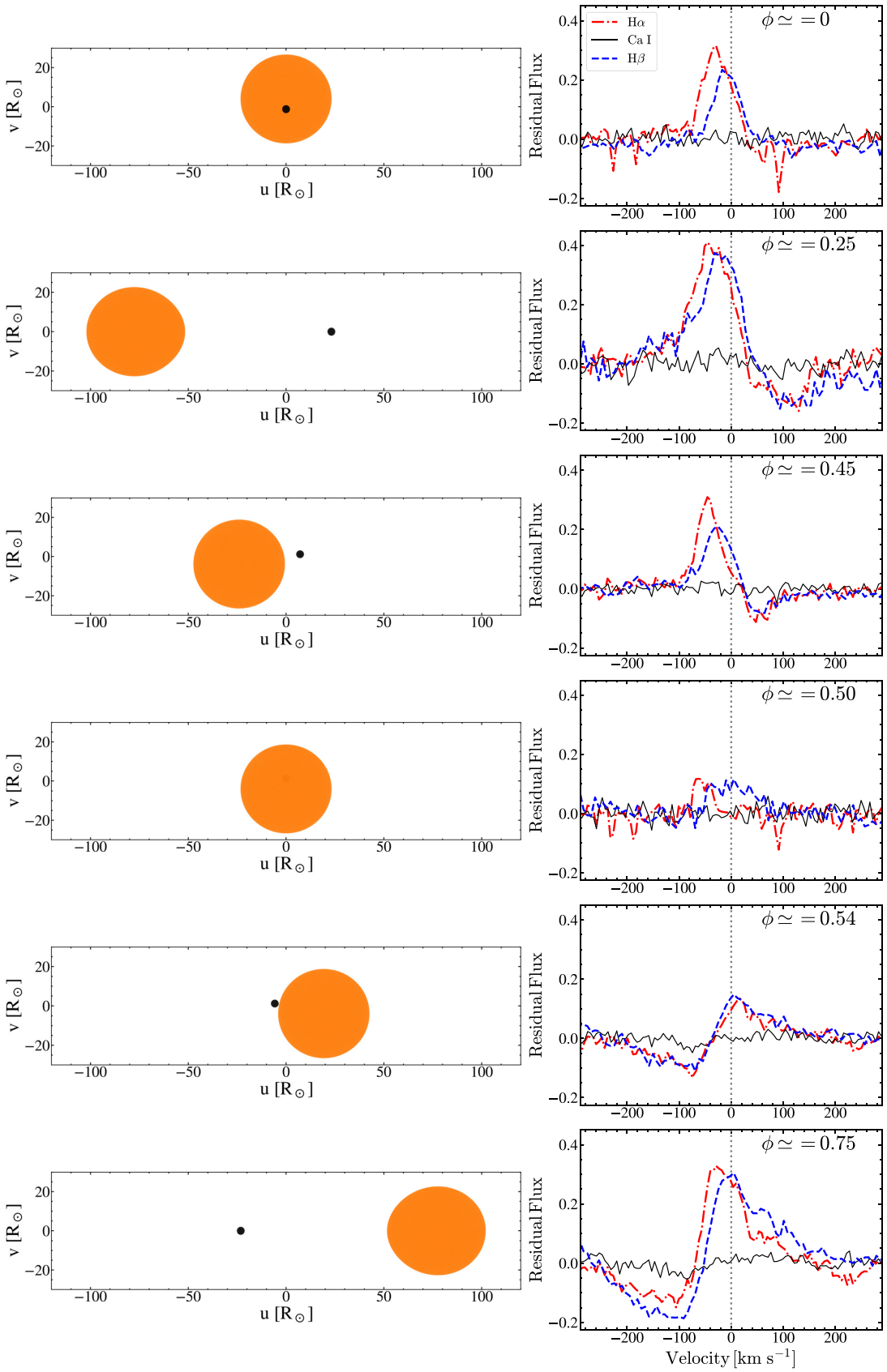

Figure 13. The right-hand panels show the template subtracted H α (red dot–dashed), H β (blue dashed), and Ca I λ6439 (black) line profiles at various orbital configurations illustrated in the left-hand panels. The size of the compact object is simply chosen to make it easily visible.

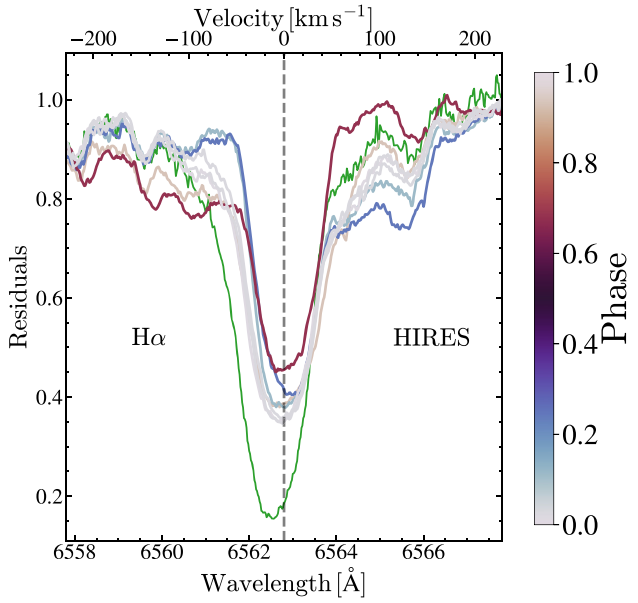

Figure 14. The HIRES Hα line profiles as a function of orbital phase. The template SES spectrum at $\phi \simeq 0.5$ is shown in green. The variability in the line profiles is the same as that seen in the SES spectra (see Fig. 11, Section 4.6).

find an upper-limit absorbed flux of 1.0×10^{-13} erg cm^{-2} s^{-1} and an unabsorbed flux of 1.1×10^{-13} erg cm^{-2} s^{-1}. Adopting the *Gaia* EDR3 distance, the latter quantity yields an X-ray luminosity upper limit of 2.7×10^{30} erg s^{-1} in the 0.5–8.0 keV band.

The *Swift* XRT estimate of the X-ray luminosity is comparable to the $L_X \sim 10^{30}$–10^{31} ergs s^{-1} observed for quiescent X-ray binaries (Dinçer et al. 2018) and the $L_X \sim 10^{29} - 10^{30}$ ergs s^{-1} observed for chromospherically active RS CVn systems (Demircan 1987). If the X-ray luminosity originates from an accretion disc, the putative BH accretes at a very low luminosity of $\sim 10^{-9}$ L_{edd}. There is observational evidence that indicates that the X-ray luminosity from quiescent BHs is significantly fainter than that from NSs (see e.g. Asai et al. 1998; Menou et al. 1999). While debated, this has been attributed to ADAF (see e.g. Narayan & Yi 1995) and the existence of event horizons for BHs. However, given the rapid rotation of the giant, some of the observed X-ray luminosity may originate from the giant's chromosphere (Gondoin 2007). The X-ray spectra of X-ray binaries are generally harder (hotter), with average temperatures $kT > 5$ keV, compared to stellar coronae that have lower temperatures, with $kT < 2$ keV (Kong et al. 2002). Given the results of the *Swift* XRT analysis, it appears that the X-ray emission is relatively soft, which appears to be consistent with a chromospheric origin. However, to fully characterize this X-ray emission, follow-up X-ray spectra of significantly better S/N are necessary.

We can estimate the mass loss rate from the giant as

$$\dot{M} = 4 \times 10^{-13}\, \eta_R\, \frac{LR}{M}\, \mathrm{M_\odot yr^{-1}} \approx 8 \times 10^{-10}\, \mathrm{M_\odot yr^{-1}}, \quad (9)$$

(Reimers 1975) where L, R, and M are in solar units and $\eta_R \simeq 0.477$ (McDonald & Zijlstra 2015). The velocity of the wind from the giant is assumed to be the escape velocity, which is $V_{wind} \approx V_{esc} \sim 120$ km s^{-1}. For a scenario where the BH accretes mass through the stellar wind, Thompson et al. (2019) approximated the amount of material gathered at the sphere of influence of the BH as

$$\dot{M}_{acc} \sim \frac{\dot{M}}{(4\pi a_{giant}^2)}\, \pi \left(\frac{G M_{BH}}{V_{wind}^2}\right)^2$$
$$\sim 7 \times 10^{-11}\, \mathrm{M_\odot\ yr^{-1}}\ \dot{M}_{-9} \left(\frac{M_{BH}}{3 \mathrm{M_\odot}}\right)^2 \left(\frac{V_{wind}}{120\ \mathrm{km\ s^{-1}}}\right)^{-4}, \quad (10)$$

where $\dot{M}_{-9} = \dot{M}/10^{-9}\, \mathrm{M_\odot\ yr^{-1}}$. For radiatively efficient accretion on to the BH, the accretion luminosity can be approximated by

$$L_{acc} \sim 0.1\, \dot{M}_{acc}\, c^2 \simeq 83\, \mathrm{L_\odot}. \quad (11)$$

For radiatively inefficient accretion, the luminosity can be much lower (Narayan & Yi 1995). This estimate of the accretion luminosity is much larger than the observed X-ray luminosity of this system (Section 4.7), but closer to the luminosity of the veiling component ($L_{acc} \approx 4 L_{veil}$).

5 THE NATURE OF THE DARK COMPANION

Given the observed properties of the system and the modelling results from Sections 3 and 4, we next systematically discuss the nature of the companion. We first discuss the uncertainties in the mass of the companion and then systematically consider the possible single and binary possibilities for its composition.

Ultimately, our knowledge of the mass of the companion is determined by how well we can constrain the properties of the giant. Estimates of the mass through either the radius and gravity or stellar evolution models give relatively crude limits of 1.1 ± 0.5 and 1.1 ± 0.2 M$_\odot$, respectively (Section 4.1). If the giant has a degenerate core, which is likely to be true because it is more luminous than the red clump, then there is a very firm lower limit to its mass. The luminosity of a giant with a degenerate core of mass M_{core} is

$$\left(\frac{L}{L_\odot}\right) \approx 675 \left(\frac{M_{core}}{0.4\ \mathrm{M_\odot}}\right)^7. \quad (12)$$

(Boothroyd & Sackmann 1988), so we must have $M_{giant} > M_{core} \simeq 0.33$ M$_\odot$ for $L \sim 170$ L$_\odot$. This implies a lower bound for the companion mass of $M_{comp} \gtrsim 2.26$ M$_\odot$, above the mass of the most massive NS observed and larger than the limits for single and binary stellar companions in Section 4.5.

The stronger limits on the mass come from the PHOEBE models of the ellipsoidal variability in Section 4.3. Ignoring inclination, ellipsoidal variability constrains the mass ratio q because (to leading order) the amplitude of the $P_{orb}/2$ term depends on $\epsilon_2 \sim (R/a)^3/q$ while the amplitudes of the P_{orb} and $P_{orb}/3$ terms depend on $(R_{giant}/a)^4/q$ (e.g. Morris 1985; Gomel, Faigler & Mazeh 2021). Since the semimajor axis is determined by the period, mass function and mass ratio, $a^3 \propto P^2 f(1+q)^2$, the ellipsoidal variability can constrain both R_{giant} and q. This also means that the radius of the giant is an important independent constraint. Given the period, mass function, and amplitude ϵ_2, the mass of the giant $M_{giant} = f q (1+q)^2 \propto R_{giant}^3$ simply scales with the radius of the giant. The mass of the companion, $M_{comp} = f(1+q)^2$, is less dependent on the radius because the mass ratio q is small. We can verify this correlation using PHOEBE models with the radius of the giant fixed to $R_{giant} = 18$, 20, 22, 24, and 26 R$_\odot$. The mass of the giant increases monotonically and fairly rapidly with radius, $M_{giant} \simeq 0.42$, 0.55, 0.72, 0.91, and 1.12 M$_\odot$, while the mass of the companion increases more slowly, $M_{comp} \simeq 2.38$, 2.55, 2.75, 2.95, and 3.16 M$_\odot$, as expected. In fact, the numerical results almost exactly track the expected scalings from holding ϵ_2 fixed while varying the radius of the star.

The PHOEBE models on their own found a radius of $R_{\rm giant} = 24.9 \pm 0.7$ R$_\odot$, which agrees well with the independent results from the SED fits. Without the correction for veiling, these fits gave 22.2 ± 0.8 R$_\odot$ and with the correction for veiling they gave 24.0 ± 0.9 R$_\odot$. These fits use a much more complete SED model than used for the *Gaia* DR2 estimate of ∼20 R$_\odot$, but even for this smaller estimate the companion mass is $M_{\rm comp} = 2.6$ M$_\odot$. Since the radius estimates from the SED and the ellipsoidal variability agree, we will proceed under the assumption that the resulting mass estimates of $M_{\rm giant} = 1.00 \pm 0.07$ M$_\odot$ and $M_{\rm comp} = 3.04 \pm 0.06$ M$_\odot$ are essentially correct.

We next consider all the possible scenarios for the composition of the companion, with Table 5 providing a summary. If the companion is a single object, the options are a star, a WD, an NS, or a BH. A star is ruled out by the eclipse and SED limits from Section 4.5, with $M_{\rm comp} < 0.8$ M$_\odot$ based on the lack of eclipses. A WD is ruled out because its mass would exceed the Chandrasekhar mass limit of 1.4 M$_\odot$. An NS is unlikely, since a companion mass of $M_{\rm comp} \simeq 3.04$ M$_\odot$ is still slightly larger than the maximum passable mass of an NS ($M \sim 3$ M$_\odot$; Lattimer & Prakash 2001). Additionally, the mass is well above the maximum observed masses of $M \simeq 2.01 \pm 0.04$ M$_\odot$ and $M \simeq 2.14^{+0.10}_{-0.09}$ M$_\odot$ found for the NSs PSR J0348+0432 and MSP J0740 + 6620, respectively (Antoniadis et al. 2013; Cromartie et al. 2020). The mass of the dark companion is slightly larger than the $M \simeq 2.59^{+0.09}_{-0.08}$ $M_\odot$ mass-gap compact object in the LIGO/VIRGO gravitational wave merger event GW190814 (Abbott et al. 2020), and it is comparable in mass to the $M_{\rm BH} \simeq 3.3^{+2.8}_{-0.7}$ M$_\odot$ non-interacting BH identified around the red giant 2MASS J05215658 + 4359220 by Thompson et al. (2019). The mass estimates for V723 Mon, due to its ellipsoidal variability, are much tighter than for 2MASS J05215658 + 4359220. Thus, the simplest explanation of observed V723 Mon system properties is that the binary companion is a BH near the lower end of the mass gap.

There are many more possible scenarios if the companion is a binary. The orbit of such a binary has to be fairly compact (see Appendix A), but not too compact, or the system would merge too rapidly (see below). While a single phase of common envelope evolution can likely lead to the simple binary models, any of these triple solutions likely requires a more complex evolutionary pathway, which we will not attempt to explore here. Based on our analyses in Section 4.5, the dark companion cannot be a stellar binary given that the two star mass limit is $M_{\rm binary} < 1.5$ M$_\odot$ from the eclipse constraints (Fig. 10). The companion must contain at least one compact object.

Combining a star with a compact object seems unlikely. With the stellar mass <0.8 M$_\odot$ based on the lack of eclipses, the compact object mass must be >2.2 M$_\odot$. A WD is ruled out because this exceeds the Chandrasekhar limit. An NS is possible, but the mass is at or above the maximum observed NS masses. A BH is also possible, but a single more massive BH seems far more plausible than a BH with an NS-like mass combined with a star to form the inner binary of a triple system.

A double WD binary requires that both WDs are very close to the Chandrasekhar limit or above it. Given that such massive WDs are quite rare (Tremblay et al. 2016), putting two of them into such a system is unlikely even if the masses can be kept just below the limit. Combining a WD and an NS is allowed, and the NS mass is in the observed range if the WD mass is >0.9 M$_\odot$. Combining a WD with a BH is possible, but has the same plausibility problems as combining a star with a BH. A double NS binary is feasible. They would need to be of similar mass, since a mass ratio >0.67 is needed to keep the lower mass NS above the theoretical minimum of 1.2 M$_\odot$ (Suwa et al. 2018). Combining an NS with a BH and a double BH binary seem implausible because they both require BH masses in the range observed for NSs.

An additional consideration for any compact object binary model for the companion is its lifetime due to the emission of gravitational waves. For an equal mass, 3 M$_\odot$ binary in a circular orbit with semimajor axis $a_{\rm in}$, the merger time is

$$t_{\rm merge} = 2.2 \times 10^7 \text{ years} \left(\frac{a_{\rm in}}{R_\odot}\right)^4 \left(\frac{3\ {\rm M}_\odot}{M_{\rm comp}}\right)^3. \quad (13)$$

If the age of the system must be >1 (10) Gyr to allow time for the red giant to evolve, then $a_{\rm in} > 2.6$ $R_\odot$ (4.6 $R_\odot$). Unfortunately, a binary with such a long lifetime is too weak a gravitational wave source to be detected by the Laser Interferometer Space Antenna (LISA, Robson, Cornish & Liu 2019). As discussed in Appendix A, dynamical stability requires $a_{\rm in} < 31$R$_\odot$ (significantly inside the Roche lobe radius of the companion, ∼49 R$_\odot$), so a long-lived, dynamically stable binary is possible for 4 R$_\odot \lesssim a_{\rm in} \lesssim 31$ R$_\odot$. This does not guarantee secular stability, and for much of this range of semimajor axes we would also expect to see dynamical perturbations of the outer orbit and additional tidal interactions (see Appendix A).

In summary, while it is difficult to rule out more complex scenarios where the companion to the giant is a binary consisting of at least one compact object, the simplest explanation is that the dark companion is a low-mass BH. This would make V723 Mon a unique system, as it would contain both the lowest mass BH in a binary and be the closest known BH yet discovered. The low X-ray luminosity ($L/L_{\rm edd} \sim 10^{-9}$) of this system likely also suggests a BH companion, as quiescent BHs are known to be X-ray faint (see Section 4.7).

6 CONCLUSIONS

The nearby ($d \simeq 460$ pc), bright ($V \simeq 8.3$ mag), evolved red giant ($T_{\rm eff,\ giant} \simeq 4440$ K, $L_{\rm giant} \simeq 173$ L$_\odot$) V723 Mon is in a high mass function, $f(M) = 1.72 \pm 0.01$ M$_\odot$, nearly circular binary ($P = 59.9$ d, $e \simeq 0$) with a dark companion of mass $M_{\rm comp} = 3.04 \pm 0.06$ M$_\odot$. V723 Mon is a known variable that had been typically classified as an eclipsing binary, but the ASAS, KELT, and *TESS* light curves indicate that is in fact a nearly edge-on ellipsoidal variable (Section 4.3, Fig. 5). We do not see any continuum eclipses in these light curves (Section 4.5, Fig. 6). Using the binary mass function and $\sin i \simeq 1$ (Section 4.3), it is clear that V723 Mon has a companion of mass 2.6 M$_\odot$ < $M_{\rm comp}$ < 3.6 M$_\odot$ for 0.5 M$_\odot$ < $M_{\rm giant}$ < 1.5 M$_\odot$. We modelled the light curves with PHOEBE using constraints on the period, RVs, and stellar temperature to derive an inclination of $i = 87.0^{\circ\,+1.7^\circ}_{-1.4^\circ}$, a mass ratio of $q \simeq 0.33 \pm 0.02$, a companion mass of $M_{\rm comp} = 3.04 \pm 0.06$ M$_\odot$, a stellar radius of $R_{\rm giant} = 24.9 \pm 0.7$ R$_\odot$, and a giant mass of $M_{\rm giant} = 1.00 \pm 0.07$ M$_\odot$ consistent with the earlier estimates (Section 4.3, Table 4).

We also identify a significant blue veiling component, both through line veiling and second light contributions to the *B*- and *V*-band light curves (Section 4.4, Fig. 9). The veiling component contributes ∼63 per cent and ∼24 per cent of the total flux in the *B* band and *V* band, respectively. The SED of the veiling component decays rapidly towards both bluer and redder wavelengths, strongly inconsistent with a stellar SED. Given that we do not see eclipses in the light curves, we infer that the veiling component has to be diffuse.

We find no evidence for a luminous stellar companion and can rule out both single and binary main sequence companions based on the SED and limits on eclipses ($M_{\rm single} < 0.80$ M$_\odot$, $M_{\rm binary} <$ 1.51 M$_\odot$) from the light curves (Section 4.5). The SED and the absence of continuum eclipses imply that the companion mass must

Table 5. Comparison of the possible scenarios involving stellar companions (∗), white dwarfs (WD), neutron stars (NS), and black holes (BH) that can explain the nature of the dark companion. We assumed $M_{\rm comp} = 3.04 \pm 0.06$ M$_\odot$ from Section 4.3 (Table 4). A '✓' indicates that the scenario is possible, a '?' indicates that while the scenario is technically possible, it is very unlikely and a '✗' indicates that the scenario is ruled out. The simplest explanation is that of a single low mass black hole, indicated with '✓✓'.

Dark companion	Possibility	Comment
Single Star	✗	Ruled out by SED/eclipse limits from Section 4.5 ($M_* \lesssim 0.8$ M$_\odot$).
Single WD	✗	WD will exceed Chandrasekhar limit ($M_{\rm WD} > 1.4$ M$_\odot$).
Single NS	?	Requires an extreme NS equation of state.
Single BH	✓✓	Simplest explanation.
Star + Star	✗	Ruled out by SED/eclipse limits from Section 4.5 ($M_{\rm binary} \lesssim 1.5$ M$_\odot$).
Star + WD	✗	For $M_* \lesssim 0.8$ M$_\odot$ (Section 4.5), the WD mass exceeds Chandrasekhar limit.
Star + NS	?	For $M_* < 0.8$ M$_\odot$, the NS mass exceeds 2.2M$_\odot$.
Star + BH	?	BH mass is even lower than with no star.
WD + WD	✗	Both WD components near or above Chandrasekhar limit.
NS + WD	✓	NS mass is in the observed range if $M_{\rm WD} > 0.9$ M$_\odot$
BH + WD	?	BH mass is even lower than with no WD.
NS + BH	✗	The BH must have an NS-like mass.
NS + NS	✓	Both NS components should have $M_{\rm NS} \gtrsim 1.2$ M$_\odot$, so $q_{\rm inner} \gtrsim 0.67$.
BH + BH	✗	The BHs have NS masses.

Table 6. Swift UVM2 observations.

JD	Date	Phase	UVM2 (mag)	σ (mag)
2459144.439	2020-10-21	0.975	14.10	0.04
2459150.607	2020-10-28	0.078	14.06	0.04
2459155.040	2020-11-01	0.152	14.07	0.04
2459158.708	2020-11-05	0.213	14.17	0.04
2459162.689	2020-11-09	0.279	14.12	0.04
2459166.865	2020-11-13	0.345	14.32	0.06
2459172.832	2020-11-19	0.449	14.10	0.04
2459173.769	2020-11-20	0.464	14.16	0.04
2459175.497	2020-11-22	0.493	14.12	0.04
2459175.753	2020-11-22	0.497	14.13	0.04
2459176.624	2020-11-23	0.512	14.13	0.04
2459184.188	2020-11-30	0.634	14.06	0.04
2459203.850	2020-12-20	0.966	14.04	0.04
2459209.830	2020-12-26	0.066	14.09	0.04
2459237.510	2021-01-23	0.528	14.07	0.04
2459240.102	2021-01-25	0.571	14.07	0.04
2459241.949	2021-01-27	0.602	14.07	0.04
2459244.948	2021-01-30	0.652	14.11	0.04
2459246.145	2021-01-31	0.672	14.03	0.04
2459249.855	2021-02-04	0.734	14.07	0.04
2459252.309	2021-02-06	0.774	14.03	0.04
2459254.172	2021-02-08	0.806	14.04	0.04
2459255.822	2021-02-10	0.833	14.06	0.04
2459259.617	2021-02-14	0.896	14.05	0.04
2459262.011	2021-02-16	0.936	14.03	0.04

be dominated by a compact object even if it is a binary (Sections 4.5 and 5, Fig. 10).

Once the spectrum of the red giant is subtracted, we also find evidence of Balmer Hα and Hβ emission (Section 4.6, Fig. 11). The morphology of the Balmer emission lines is complicated, and its origin is unclear. Even though we observe eclipses of the Balmer lines when the dark companion passes behind the giant, the velocity scales seem too low to be associated with an accretion disc. We also detect this system in the X-rays with $L_{\rm X} \simeq 7.6 \times 10^{29}$ ergs s^{-1} ($L/L_{\rm edd} \sim 10^{-9}$) using *Swift* XRT data (Section 4.7).

The simplest explanation for the dark companion is a single compact object, most likely a BH, in the 'mass gap', making V723 Mon the host to the closest BH yet discovered (Section 5, Table 5). Prior to this discovery, A0620-00 (V616 Mon) was the closest confirmed BH at an estimated distance of ∼1.6 kpc (Gelino, Harrison & Orosz 2001). However, more exotic scenarios can also be plausible explanations, including an NS–NS binary and a WD–NS binary.

To better understand this unique system, further comprehensive multiwavelength observations are necessary. In particular, UV observations from the *Hubble* space telescope will constrain the nature of the veiling component, and X-ray light curves will be useful to understand the nature of the compact object in this system. Future data releases from *Gaia* will also confirm the orbital inclination.

We can very crudely estimate the expected number of similar systems based on the fraction of the thin disc mass from which V723 Mon was selected. We assume a simple exponential disc model with density

$$\rho = \rho_0 \, e^{-R/R_d - |z|/h}, \tag{14}$$

where $R_{\rm d} \approx 3$ kpc is the disc scale length (Amôres, Robin & Reylé 2017) and the numerical values of the disc scale height h and density normalization ρ_0 are not needed. The total disc mass is $4\pi\rho_0 h R_{\rm d}^2$. If we assume that V723 Mon was selected from a cylinder of radius R at the Galactocentric radius of the Sun, $R_\odot \simeq 8$ kpc (Gravity Collaboration 2019; Stanek & Garnavich 1998), the survey examined a mass of approximately $4\pi h R^2 \exp(-R_{\rm sun}/R_{\rm d})$, so the fraction of the disc mass surveyed is approximately

$$\left(\frac{R}{R_{\rm d}}\right)^2 \exp(-R_{\rm sun}/R_{\rm d}) \simeq 0.008, \tag{15}$$

if we assume $R \simeq 1$ kpc, as this encompasses most of the systems in the SB9 catalogue. The fraction drops to 0.002 if we use the distance $R \simeq 0.5$ kpc to V723 Mon. This implies that the Galaxy might contain some 100–1000 similar systems. Since ellipsoidal variability is only possible for a limited range of semimajor axes, it is not surprising that this estimate is larger than the number of mass transfer systems but smaller than estimates of the total number (10^3–10^4) of non-interacting BH binaries in the Galaxy based on population synthesis models (see e.g. Breivik et al. 2017; Shao & Li 2019).

A number of large spectroscopy projects such as APOGEE (Majewski et al. 2017) and LAMOST (Cui et al. 2012) are in

Table 7. STELLA RV observations.

BJD	Phase	RV (kms^{-1})	σ_{RV} (kms^{-1})
2454065.57926	0.242	− 63.359	0.243
2454066.65035	0.260	− 63.407	0.199
2454073.62965	0.376	− 47.100	0.667
2454073.66318	0.377	− 43.862	0.305
2454092.53351	0.692	61.584	0.199
2454096.49062	0.758	66.656	0.104
2454101.53952	0.842	58.195	0.166
2454106.54614	0.926	34.825	0.288
2454110.49315	0.991	8.326	0.633
2454116.54293	0.092	− 34.096	0.191
2454119.51924	0.142	− 48.571	0.782
2454122.50426	0.192	− 58.969	0.199
2454125.53651	0.242	− 63.511	0.229
2454134.55945	0.393	− 40.037	0.199
2454146.52391	0.592	35.495	0.177
2454147.48687	0.609	41.043	0.246
2454152.52001	0.693	61.471	0.142
2454162.44243	0.858	54.887	0.153
2454209.37594	0.641	50.398	0.692
2454359.72466	0.149	− 50.362	0.294
2454364.72854	0.233	− 63.249	0.217
2454369.71403	0.316	− 57.753	0.264
2454377.71952	0.450	− 19.751	0.245
2454380.69831	0.499	0.271	0.21
2454383.73052	0.550	20.050	0.215
2454388.73313	0.633	48.436	0.228
2454393.70367	0.716	64.911	0.191
2454405.66540	0.916	38.520	0.221
2454420.72099	0.167	− 54.873	0.242
2454439.66728	0.483	− 7.008	0.146
2454455.56730	0.748	67.228	0.144
2454460.61450	0.833	59.969	0.138
2454462.62496	0.866	52.822	0.163
2454465.56605	0.915	38.728	0.214
2454467.57168	0.949	26.208	0.212
2454474.52033	0.065	− 23.485	0.115
2454480.53118	0.165	− 54.127	0.16
2454491.51022	0.348	− 51.196	0.239
2454497.51601	0.448	− 20.500	0.175
2454507.49658	0.615	42.842	0.177
2454532.44126	0.031	− 10.068	0.107
2454562.37656	0.530	12.045	0.183
2454711.73134	0.022	− 5.892	0.171
2454712.73270	0.039	− 13.559	0.17
2454713.72543	0.055	− 20.512	0.196
2454714.72726	0.072	− 26.952	0.15
2454722.70809	0.205	− 60.739	0.196
2454725.73812	0.256	− 63.261	0.225
2454730.74308	0.339	− 53.547	0.235
2454746.71606	0.606	40.325	0.148
2454753.62038	0.721	65.033	0.113
2454762.70971	0.873	51.111	0.195
2454777.67078	0.122	− 43.374	0.194
2454779.70948	0.156	− 52.195	0.205
2454781.55314	0.187	− 58.178	0.45
2454804.64456	0.572	28.742	0.251
2454811.50714	0.687	60.808	0.145
2454871.42332	0.686	60.469	0.176
2454872.43280	0.703	63.085	0.185
2454928.39897	0.637	49.463	0.154
2455170.50320	0.676	58.817	0.164
2455170.54417	0.677	58.970	0.18
2455171.68616	0.696	62.342	0.166
2455172.48258	0.709	64.109	0.091
2455172.66102	0.712	64.566	0.118
2455204.57655	0.244	− 63.338	0.167
2455208.54129	0.311	− 58.753	0.153
2455209.59017	0.328	− 55.705	0.195
2455210.52913	0.344	− 52.276	0.203
2455211.48735	0.360	− 48.608	0.205
2455212.58559	0.378	− 43.778	0.195
2455213.43953	0.392	− 39.561	0.214
2455214.46909	0.409	− 34.428	0.193
2455215.50881	0.427	− 28.606	0.167
2455216.46226	0.443	− 22.608	0.142
2455218.48622	0.476	− 9.364	0.136
2455220.51537	0.510	4.421	0.138
2455222.51638	0.544	17.986	0.141
2455224.54100	0.577	30.681	0.172
2455231.52035	0.694	62.259	0.143
2455238.50895	0.811	63.532	0.172
2455239.46454	0.826	61.403	0.221
2455240.50720	0.844	58.147	0.139
2455266.45443	0.277	− 62.580	0.148
2455285.40569	0.593	36.069	0.148
2455290.39565	0.676	58.852	0.114
2455297.37772	0.793	65.281	0.144

the process of physically characterizing (kinematics, temperature, abundances, etc.) millions of Galactic stars. These surveys frequently obtain their spectra in multiple visits, providing sparse RV curves for huge numbers of stars. A particularly important synergy is the ability to combine photometric surveys with these spectroscopic surveys to search for non-interacting compact object binaries like V723 Mon. For example, for the vast majority of these relatively bright stars, the ASAS-SN survey (Shappee et al. 2014; Kochanek et al. 2017; Jayasinghe et al. 2018, 2021) will supply all-sky, well-sampled light curves spanning multiple years. If we make a conservative assumption that ASAS-SN can characterize the variability of most giants up to ∼3 kpc away (not accounting for extinction), there may be ∼20 red giants with non-interacting companions that have ASAS-SN light curves. However, there is a significant cost to confirming these systems. In particular, a well-sampled set of RV measurements is required to accurately measure the mass function and to constrain the properties of any companion. None the less, as the spectroscopic surveys expand from a few 10^5 to a few 10^6 stars during the next 5 yr, this approach will become a major probe of compact object binaries.

ACKNOWLEDGEMENTS

We thank the referee, Dr. Jerome Orosz, for his useful comments on this manuscript.

We thank Dr. Jennifer Johnson, Dr. Marc Pinsonneault, Dr. Jim Fuller, and Dr. Kento Masuda for useful discussions on this manuscript. We thank Dr. Jay Strader for a careful reading of this manuscript. We thank Dr. Rick Pogge for his help with obtaining the LBT/MODS spectra.

The ASAS-SN team at OSU is supported by the Gordon and Betty Moore Foundation through grant GBMF5490 to the Ohio State University, and NSF grant AST-1908570.

TJ, KZS, and CSK are supported by NSF grants AST-1814440 and AST-1908570. TJ acknowledges support from the Ohio State Presidential Fellowship. TAT is supported in part by NASA grant

Table 8. Spectroscopic observations from HIRES, MODS, and PEPSI.

BJD [TDB]	Date	Phase	RV (kms^{-1})	σ_{RV} (kms^{-1})	Instrument
2459143.09532	2020-10-20	0.952	24.39	0.10	HIRES
2459153.99899	2020-10-31	0.134	−47.28	0.10	HIRES
2459162.02289	2020-11-08	0.268	−63.27	0.10	HIRES
2459188.01112	2020-12-04	0.702	62.67	0.10	HIRES
2459208.01826	2020-12-24	0.036	−12.23	0.10	HIRES
2459208.89679	2020-12-25	0.050	−17.51	0.10	HIRES
2459209.98247	2020-12-26	0.068	−24.92	0.10	HIRES
2459171.94982	2020-11-18	0.434	—	—	MODS
2459173.86921	2020-11-20	0.466	—	—	MODS
2459174.89034	2020-11-21	0.483	—	—	MODS
2459175.77657	2020-11-22	0.498	—	—	MODS
2459183.77896	2020-11-30	0.631	48.74	0.25	PEPSI

80NSSC20K0531. TAT acknowledges previous support from Scialog Scholar grant 24216 from the Research Corporation, from which this effort germinated. JTH is supported by NASA award 80NSSC21K0136. Support for JLP is provided in part by the Ministry of Economy, Development, and Tourism's Millennium Science Initiative through grant IC120009, awarded to The Millennium Institute of Astrophysics, MAS. DH acknowledges support from the Alfred P. Sloan Foundation, the National Aeronautics and Space Administration (80NSSC18K1585, 80NSSC19K0379), and the National Science Foundation (AST-1717000). CB acknowledges support from the National Science Foundation grant AST-1909022.

Parts of this research were supported by the Australian Research Council Centre of Excellence for All Sky Astrophysics in 3 Dimensions (ASTRO 3D), through project number CE170100013.

The LBT is an international collaboration among institutions in the United States, Italy and Germany. LBT Corporation partners are as follows: The University of Arizona on behalf of the Arizona Board of Regents; Istituto Nazionale di Astrofisica, Italy; LBT Beteiligungsgesellschaft, Germany, representing the Max-Planck Society, The Leibniz Institute for Astrophysics Potsdam, and Heidelberg University; The Ohio State University, representing OSU, University of Notre Dame, University of Minnesota, and University of Virginia.

STELLA and PEPSI were made possible by funding through the State of Brandenburg (MWFK) and the German Federal Ministry of Education and Research (BMBF) through their Verbundforschung grants 05AL2BA1/3 and 05A08BAC.

This research is based on observations made with the *Neil Gehrels Swift Observatory*, obtained from the MAST data archive at the Space Telescope Science Institute, which is operated by the Association of Universities for Research in Astronomy, Inc., under NASA contract NAS 5-26555. This paper includes data collected with the *TESS* mission, obtained from the MAST data archive at the Space Telescope Science Institute (STScI). Funding for the *TESS* mission is provided by the NASA Explorer Program. STScI is operated by the Association of Universities for Research in Astronomy, Inc., under NASA contract NAS 5-26555.

Some of the data presented herein were obtained at the W. M. Keck Observatory, which is operated as a scientific partnership among the California Institute of Technology, the University of California and the National Aeronautics and Space Administration. The Observatory was made possible by the generous financial support of the W. M. Keck Foundation.

The authors wish to recognize and acknowledge the very significant cultural role and reverence that the summit of Maunakea has always had within the indigenous Hawaiian community. We are most fortunate to have the opportunity to conduct observations from this mountain.

We thank the ASAS and KELT projects for making their light-curve data publicly available. This research has used the VizieR catalogue access tool, CDS, Strasbourg, France. This research also used ASTROPY, a community-developed core PYTHON package for Astronomy (Astropy Collaboration 2013, 2018).

DATA AVAILABILITY

The data underlying this article will be shared on reasonable request to the corresponding author.

REFERENCES

Abbott B. P. et al., 2016, Phys. Rev. Lett., 116, 061102
Abbott B. P. et al., 2017, Phys. Rev. Lett., 119, 161101
Abbott R. et al., 2020, ApJ, 896, L44
Abdul-Masih M. et al., 2020, Nature, 580, E11
Adams S. M., Kochanek C. S., 2015, MNRAS, 452, 2195
Alard C., 2000, A&AS, 144, 363
Amôres E. B., Robin A. C., Reylé C., 2017, A&A, 602, A67
Antoniadis J. et al., 2013, Science, 340, 448
Arras P., Burkart J., Quataert E., Weinberg N. N., 2012, MNRAS, 422, 1761
Asai K., Dotani T., Hoshi R., Tanaka Y., Robinson C. R., Terada K., 1998, PASJ, 50, 611
Astropy Collaboration, 2013, A&A, 558, A33
Astropy Collaboration, 2018, AJ, 156, 123
Bailer-Jones C. A. L., Rybizki J., Fouesneau M., Mantelet G., Andrae R., 2018, AJ, 156, 58
Beech M., 1985, Ap&SS, 117, 69
Blanco-Cuaresma S., 2019, MNRAS, 486, 2075
Blanco-Cuaresma S., Soubiran C., Heiter U., Jofré P., 2014, A&A, 569, A111
Bodensteiner J. et al., 2020, A&A, 641, A43
Boothroyd A. I., Sackmann I.-J., 1988, ApJ, 328, 641
Breeveld A. A. et al., 2010, MNRAS, 406, 1687
Breivik K., Chatterjee S., Larson S. L., 2017, ApJ, 850, L13
Bressan A., Marigo P., Girardi L., Salasnich B., Dal Cero C., Rubele S., Nanni A., 2012, MNRAS, 427, 127
Brown T. M., Gilliland R. L., Noyes R. W., Ramsey L. W., 1991, ApJ, 368, 599
Burrows D. N. et al., 2005, Space Sci. Rev., 120, 165
Cardelli J. A., Clayton G. C., Mathis J. S., 1989, ApJ, 345, 245
Casares J., Charles P. A., Naylor T., Pavlenko E. P., 1993, MNRAS, 265, 834
Castelli F., Kurucz R. L., 2003, in Piskunov N., Weiss W. W., Gray D. F., eds, Proc. IAU Symp. 210, Modelling of Stellar Atmospheres. Kluwer, Dordrecht, p. A20
Champion D. J. et al., 2008, Science, 320, 1309

Choi J., Dotter A., Conroy C., Cantiello M., Paxton B., Johnson B. D., 2016, ApJ, 823, 102
Claret A., Bloemen S., 2011, A&A, 529, A75
Conroy K. E. et al., 2020, ApJS, 250, 34
Cromartie H. T. et al., 2020, Nat. Astron., 4, 72
Cui X.-Q. et al., 2012, Res. Astron. Astrophys., 12, 1197
Demircan O., 1987, Ap&SS, 137, 195
Dinçer T., Bailyn C. D., Miller-Jones J. C. A., Buxton M., MacDonald R. K. D., 2018, ApJ, 852, 4
Dotter A., 2016, ApJS, 222, 8
Eastman J., Siverd R., Gaudi B. S., 2010, PASP, 122, 935
Eaton J. A., 2008, ApJ, 681, 562
El-Badry K., Quataert E., 2020, MNRAS, 493, L22
El-Badry K., Quataert E., 2021, MNRAS, 502, 3436
Elitzur M., Ivezić Ž., 2001, MNRAS, 327, 403
ESA, 1997, VizieR Online Data Catalog. p. I/239
Esin A. A., McClintock J. E., Narayan R., 1997, ApJ, 489, 865
Farr W. M., Sravan N., Cantrell A., Kreidberg L., Bailyn C. D., Mandel I., Kalogera V., 2011, ApJ, 741, 103
Foreman-Mackey D., Hogg D. W., Lang D., Goodman J., 2013, PASP, 125, 306
Gabriel C. et al., 2004, in Ochsenbein F., Allen M. G., Egret D., eds, ASP Conf. Ser. Vol. 314, Astronomical Data Analysis Software and Systems (ADASS) XIII, The XMM–Newton SAS - Distributed Development and Maintenance of a Large Science Analysis System: A Critical Analysis. Astron. Soc. Pac., San Francisco, p. 759
Gagné J. et al., 2018, ApJ, 856, 23
Gahm G. F., Walter F. M., Stempels H. C., Petrov P. P., Herczeg G. J., 2008, A&A, 482, L35
Gaia Collaboration, 2018, A&A, 616, A1
Gaia Collaboration, 2020, A&A, preprint (arXiv:2012.01533)
Gelino D. M., Harrison T. E., Orosz J. A., 2001, AJ, 122, 2668
Giesers B. et al., 2018, MNRAS, 475, L15
Giesers B. et al., 2019, A&A, 632, A3
Gomel R., Faigler S., Mazeh T., 2021, MNRAS, 501, 2822
Gondoin P., 2007, A&A, 464, 1101
Gontcharov G. A., Mosenkov A. V., 2017, MNRAS, 472, 3805
González Hernández J. I., Casares J., 2010, A&A, 516, A58
Gräfener G., Owocki S. P., Vink J. S., 2012, A&A, 538, A40
Gravity Collaboration, 2019, A&A, 625, L10
Gray R. O., Corbally C. J., 1994, AJ, 107, 742
Green G. M., Schlafly E., Zucker C., Speagle J. S., Finkbeiner D., 2019, ApJ, 887, 93
Griffin R. F., 2010, The Observatory, 130, 60
Griffin R. F., 2014, The Observatory, 134, 109 (G14)
Gustafsson B., Edvardsson B., Eriksson K., Jørgensen U. G., Nordlund, Å., Plez B., 2008, A&A, 486, 951
Hall J. C., 1996, PASP, 108, 313
Hambsch F. J., 2012, J. Am. Assoc. Variable Star Observers, 40, 1003
Henden A. A., Levine S., Terrell D., Welch D. L., Munari U., Kloppenborg B. K., 2018, American Astronomical Society Meeting Abstracts #232. p. 223.06
Hill G., Fisher W. A., Holmgren D., 1989, A&A, 218, 152
Horvat M., Conroy K. E., Pablo H., Hambleton K. M., Kochoska A., Giammarco J., Prša A., 2018, ApJS, 237, 26
Houk N., Swift C., 2000, VizieR Online Data Catalog. p. III/214
Howard A. W. et al., 2010, ApJ, 721, 1467
Hynes R. I., Robinson E. L., Bitner M., 2005, ApJ, 630, 405
Irrgang A., Geier S., Kreuzer S., Pelisoli I., Heber U., 2020, A&A, 633, L5
Ivezic Z., Elitzur M., 1997, MNRAS, 287, 799
Jansen F. et al., 2001, A&A, 365, L1
Jayasinghe T. et al., 2018, MNRAS, 477, 3145
Jayasinghe T. et al., 2021, MNRAS, 503, 200
Kanodia S., Wright J., 2018, Res. Notes Am. Astron. Soc., 2, 4
Kazarovets E. V., Samus N. N., Durlevich O. V., Frolov M. S., Antipin S. V., Kireeva N. N., Pastukhova E. N., 1999, Information Bulletin on Variable Stars, No. 4659, #1
Kjeldsen H., Bedding T. R., 1995, A&A, 293, 87
Kochanek C. S. et al., 2017, PASP, 129, 104502
Kong A. K. H., McClintock J. E., Garcia M. R., Murray S. S., Barret D., 2002, ApJ, 570, 277
Kurucz R. L., 1993, SYNTHE Spectrum Synthesis Programs And Line Data
Lagarias J., Reeds J., Wright M., Wright P., 1998, SIAM J. Optim., 9, 112
Lattimer J. M., Prakash M., 2001, ApJ, 550, 426
Lenz P., Breger M., 2005, Commun. Asteroseismol., 146, 53
Liszt H., 2014, ApJ, 780, 10
Liu J. et al., 2019, Nature, 575, 618
Liu Q. Z., van Paradijs J., van den Heuvel E. P. J., 2006, A&A, 455, 1165
López-Santiago J., Montes D., Gálvez-Ortiz M. C., Crespo-Chacón I., Martínez-Arnáiz R. M., Fernández-Figueroa M. J., de Castro E., Cornide M., 2010, A&A, 514, A97
Majewski S. R. et al., 2017, AJ, 154, 94
Mardling R. A., Aarseth S. J., 2001, MNRAS, 321, 398
McDonald I., Zijlstra A. A., 2015, MNRAS, 448, 502
Menou K., Esin A. A., Narayan R., Garcia M. R., Lasota J.-P., McClintock J. E., 1999, ApJ, 520, 276
Mészáros S. et al., 2012, AJ, 144, 120
Morris S. L., 1985, ApJ, 295, 143
Morton T. D., 2015, Astrophysics Source Code Library, record ascl:1503.01
Narayan R., Yi I., 1995, ApJ, 452, 710
Neilsen J., Steeghs D., Vrtilek S. D., 2008, MNRAS, 384, 849
Noyes R. W., Hartmann L. W., Baliunas S. L., Duncan D. K., Vaughan A. H., 1984, ApJ, 279, 763
Onken C. A. et al., 2019, Publ. Astron. Soc. Aust., 36, e033
Orosz J. A., Hauschildt P. H., 2000, A&A, 364, 265
Papaj J., Krelowski J., Wegner W., 1993, A&A, 273, 575
Penoyre Z., Stone N. C., 2019, AJ, 157, 60
Pepper J. et al., 2007, PASP, 119, 923
Petigura E. A., 2015, PhD thesis, Univ. California
Pinsonneault M. H. et al., 2018, ApJS, 239, 32
Pogge R. W. et al., 2010, Ground-based and Airborne Instrumentation for Astronomy III. p. 77350A
Pojmanski G., 1997, Acta Astron., 47, 467
Pojmanski G., 2002, Acta Astron., 52, 397
Poole T. S. et al., 2008, MNRAS, 383, 627
Pourbaix D. et al., 2004, A&A, 424, 727
Poznanski D., Prochaska J. X., Bloom J. S., 2012, MNRAS, 426, 1465
Price-Whelan A. M., Goodman J., 2018, ApJ, 867, 5
Price-Whelan A. M., Hogg D. W., Foreman-Mackey D., Rix H.-W., 2017, ApJ, 837, 20
Prša A. et al., 2016, ApJS, 227, 29
Quataert E., Narayan R., 1999, ApJ, 520, 298
Ramírez I., Allende Prieto C., Lambert D. L., 2013, ApJ, 764, 78
Reimers D., 1975, Mem. Soc. R. Sci. Liege, 8, 369
Ricker G. R. et al., 2015, J. Astron. Telesc. Instrum. Syst., 1, 014003
Rivinius T., Baade D., Hadrava P., Heida M., Klement R., 2020, A&A, 637, L3
Robson T., Cornish N. J., Liu C., 2019, Class. Quantum Gravity, 36, 105011
Roming P. W. A. et al., 2005, Space Sci. Rev., 120, 95
Schönrich R., Binney J., Dehnen W., 2010, MNRAS, 403, 1829
Shahbaz T., Russell D. M., Zurita C., Casares J., Corral-Santana J. M., Dhillon V. S., Marsh T. R., 2013, MNRAS, 434, 2696
Shao Y., Li X.-D., 2019, ApJ, 885, 151
Shappee B. J. et al., 2014, ApJ, 788, 48
Shenar T. et al., 2020, A&A, 639, L6
Siverd R. J. et al., 2012, ApJ, 761, 123
Skrutskie M. F. et al., 2006, AJ, 131, 1163
Sneden C., 1973, ApJ, 184, 839
Soderblom D. R., Stauffer J. R., Hudon J. D., Jones B. F., 1993, ApJS, 85, 315
Stanek K. Z., Garnavich P. M., 1998, ApJ, 503, L131
Stassun K. G. et al., 2019, AJ, 158, 138
Strader J. et al., 2015, ApJ, 804, L12
Straizys V., Kuriliene G., 1981, Ap&SS, 80, 353
Strassmeier K. G. et al., 2015, Astron. Nachr., 336, 324

Strassmeier K. G., Weber M., Granzer T., Järvinen S., 2012, Astron. Nachr., 333, 663 (S12)
Strassmeier K. G., Ilyin I., Steffen M., 2018, A&A, 612, A44
Suwa Y., Yoshida T., Shibata M., Umeda H., Takahashi K., 2018, MNRAS, 481, 3305
Swihart S. J. et al., 2018, ApJ, 866, 83
Ter Braak C. J. F., 2006, Stat. Comput., 16, 239
Thompson T. A. et al., 2019, Science, 366, 637
Tremblay P.-E., Cummings J., Kalirai J. S., Gänsicke B. T., Gentile-Fusillo N., Raddi R., 2016, MNRAS, 461, 2100
Tsantaki M., Andreasen D. T., Teixeira G. D. C., Sousa S. G., Santos N. C., Delgado-Mena E., Bruzual G., 2018, MNRAS, 473, 5066
Tsantaki M., Andreasen D., Teixeira G., 2020, J. Open Source Softw., 5, 2048
Vallely P. J., Kochanek C. S., Stanek K. Z., Fausnaugh M., Shappee B. J., 2021, MNRAS, 500, 5639
van Belle G. T. et al., 1999, AJ, 117, 521
Verbunt F., Phinney E. S., 1995, A&A, 296, 709
Vogt S. S. et al., 1994, in Crawford D. L., Craine E. R., eds, Proc. SPIE Conf. Ser., Vol. 2198, Instrumentation in Astronomy VIII. SPIE, Bellingham, p. 362
Wagner R. M., Kreidl T. J., Howell S. B., Starrfield S. G., 1992, ApJ, 401, L97
Watson C. L., Henden A. A., Price A., 2006, in The Society for Astronomical Sciences 25th Annual Symposium on Telescope Science, Society for Astronomical Sciences, p. 47
Weber M., Granzer T., Strassmeier K. G., Woche M., 2008, in Bridger A., Radziwill N. M., eds, Proc. SPIE Conf. Ser., Vol. 7019, Advanced Software and Control for Astronomy II. SPIE, Bellingham, p. 70190L
Wilson R. E., Sofia S., 1976, ApJ, 203, 182
Wright E. L. et al., 2010, AJ, 140, 1868
Wu J. et al., 2015, ApJ, 806, 92
Zurita C., Casares J., Shahbaz T., 2003, ApJ, 582, 369
Özel F., Psaltis D., Narayan R., McClintock J. E., 2010, ApJ, 725, 1918

APPENDIX A: THE ORIGIN OF THE RADIAL VELOCITY RESIDUALS

S12 interpreted V723 Mon as a triple system where the companion is a binary with period $P_{\rm in} = P_{\rm orb}/3 \simeq 20$ d. G14 argued against this hypothesis, but there are significant RV residuals at $P_{\rm orb}/2$ or $P_{\rm orb}/3$ depending on whether the model for the orbit of the giant is circular or elliptical (see Section 4.2 and Fig 3). We know from the limits on stellar companions in Section 4.5 that a star cannot dominate the mass of the companion, but there are also two independent arguments against any such binary, stellar or not. We do, however, have a hypothesis for the origin of these RV residuals.

The first argument against a ∼20 d inner binary is the dynamical stability argument raised by G14. For our nominal parameters, the outer orbit has a total mass of $\simeq 4\,{\rm M}_\odot$ (in round numbers) and a semimajor axis of 100 $\rm R_\odot$ while the inner orbit has a mass of 3 $\rm M_\odot$. The 45 $\rm R_\odot$ semimajor axis of a 20 d binary is very close to the Roche limit around the companion of 49 $\rm R_\odot$. A rough estimate of the largest semimajor axis that could be dynamically stable given the outer orbit and the mass ratios is 32 $\rm R_\odot$ based on Mardling & Aarseth (2001). In short, G14 was correct to hypothesize that such an orbit should be dynamically unstable.

We experimented with numerically integrating planar three-body orbits starting from nominally circular orbits as initial conditions for ∼100 orbits of the outer binary and varying mass ratios of the inner binary. High mass ratio inner binaries were generally very unstable, presumably because the lighter star in the inner binary is trying to maintain an orbital radius close to the full semimajor axis of 45 $\rm R_\odot$ in this limit. Equal mass inner binaries tended to be more stable, presumably because each star now only has an orbit of ∼23 $\rm R_\odot$ about the centre of mass of the inner binary. Nonetheless, many trials resulted in the destruction of the system well before 100 orbits were completed. These results were not unique to picking a truly resonant $P_{\rm orb}/3$ period for the inner binary. We suspect, but do not investigate here, that essentially all such inner binaries are unstable on long time-scales. The inner binary would have to have a period shorter than ∼12 d to satisfy the dynamical stability criterion, although such systems may still be secularly unstable.

The other problem with longer period inner binaries is that they perturb the outer orbit and produce time varying tidal forces on the giant even if stable. In particular, the wider inner binaries would generally drive the outer orbit to be significantly elliptical in our numerical experiments even if they were stable over the 100 orbits. Making the companion a binary also means that the tidal forces on the giant are time variable. If the companion is a single star, the amplitude of the elliptical variability depends on $(R_{\rm giant}/a)^3$ while if it is an equal mass binary it depends on

$$\frac{x}{2}\left(\frac{R_{\rm giant}}{d_1}\right)^2 + \frac{1-x}{2}\left(\frac{R_{\rm giant}}{d_2}\right)^3, \tag{A1}$$

where d_1 and d_2 are the distances to the two stars that comprise fractions x and $1-x$ of the mass of the inner binary. Compared to a single companion, there is a fractional fluctuating tidal amplitude for circular orbits of order

$$3\,(1-2x)\,\frac{a_{\rm in}}{a}\cos\omega_t t + \frac{15}{4}\left(1-3x+3x^2\right)\frac{a_{\rm in}^2}{a^2}\cos 2\omega_t t, \tag{A2}$$

where the frequency $\omega_t = \omega_{\rm in} - \omega$ is the frequency difference between the inner and outer binaries. In particular, for an equal mass ($x = 1/2$) inner binary, the peak-to-peak fractional change in the tidal forcing is

$$\frac{15}{8}\left(\frac{a_{\rm in}}{a}\right)^2, \tag{A3}$$

so a $P_{\rm in} = 20$ d period inner binary would produce ∼ 38 per cent peak-to-peak fluctuations in the tidal force with a period of 15 d. No such residuals are seen in the residuals from the ellipsoidal model of the light curves at this or any similar period (see Appendix B). To have fractional fluctuations in the tidal forcing smaller than $f = 0.1 f_{10}$ requires an equal mass inner binary to be more compact than $a_{\rm in} < 23 f_{10}^{1/2} \rm R_\odot$ and to have a period $P_{\rm in} < 7.4 f_{10}^{3/2}$ d.

These arguments appear to strongly rule out the inner binary proposed by S12. We instead suspect that the RV residuals and much of the evidence for a binary companion are driven by the consequences of making RV observations of a high amplitude ELL variable. This effect has previously been discussed (Hill, Fisher & Holmgren 1989; Eaton 2008) in the context of contact/semidetached eclipsing binaries and ellipsoidal variables in close orbits (Wilson & Sofia 1976). The very similar issues for observations of stars with dynamical tides have also been discussed (e.g. Arras et al. 2012, Penoyre & Stone 2019) recently.

A tidally locked star is simply rotating at the orbital frequency, so the rotation velocity at the surface scales with the cylindrical radius from the rotation axis. Thus, the rotational velocity is larger on the long axis of the star than on the short axis. When viewed along a principal axis, there is the usual cancellation of the contributions from the parts of the star rotating towards and away from the observer. However, when viewed at an intermediate direction, the contribution of one sign of the rotation comes from the slower moving short axis, while the contribution from the other sign comes from the faster moving long axis. This makes a contribution to the observed radial velocities with a period $P_{\rm orb}/2$ because it is a $m = 2$ perturbation just

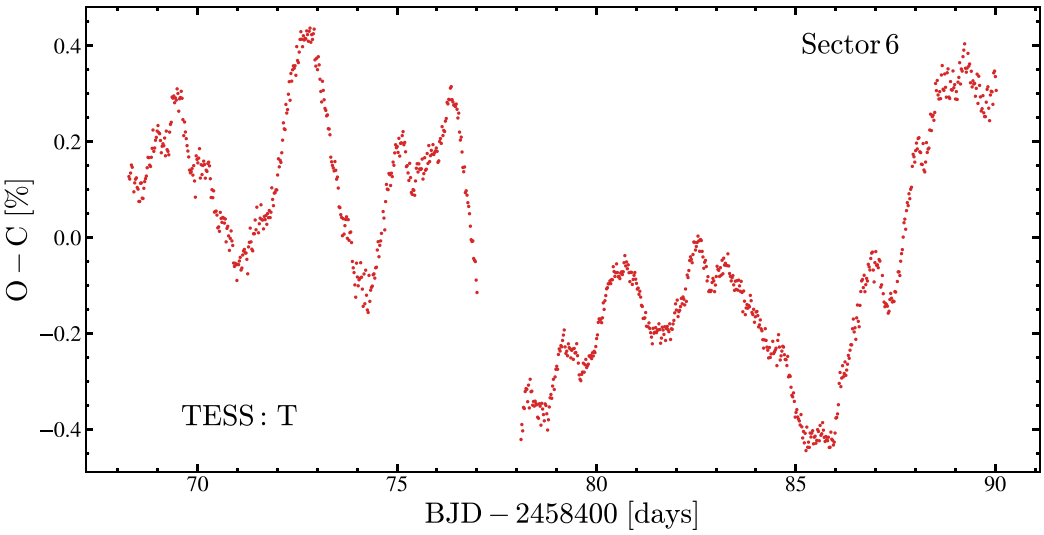

Figure B1. The light curve residuals for the *TESS* sector 6 data after the PHOEBE model is subtracted.

like the tidal distortions. If the orbit is genuinely circular, a fit to the RV curve will instead yield a small eccentricity to try to remove the contribution from this effect (see Eaton 2008). This should mean that the dominant velocity residual will now have a period $P_{\rm orb}/3$, and we think this is the likely origin of the $P_{\rm orb}/3$ signal found by Strassmeier et al. (2012).

APPENDIX B: SHORT TIME-SCALE VARIABILITY

We searched for additional variability on three broad time-scales. First, we looked for extra variability on the time-scales of weeks or longer in the residuals of the ASAS and KELT light curves after subtracting the best model for the ellipsoidal variability. Next, we looked for variability on the time-scale of days in the residuals of the *TESS* light curve. Finally, we searched for very short time-scale variability during several periods of very high cadence ROAD observations.

As discussed in Appendix A, a sufficiently wide binary secondary will produce strong fluctuations in the strength of the tides on the giant at periods with frequencies that are either the difference in frequency between the inner and outer binary w_t or twice that frequency, with the perturbations at w_t requiring an un-equal mass binary companion. In particular, for the 20 d period inner binary proposed by S12, we would expect strong fluctuating tides on periods of 30 and 15 d, although the 30 d period could be partly absorbed into the ELL fit. We looked for periodic signals in the residuals of the fits to the ASAS and KELT light curves using `Period04` (Lenz & Breger 2005), and found none that were significant (an S/N > 5). Given the level of the residuals and the expected amplitude of the perturbations for a 20 d inner binary, this appears to strongly rule out such a companion.

We see clear evidence of structure in the *TESS* residuals on short time-scales (Fig. B1) with an amplitude of 0.4 per cent. At least in this short *TESS* light curve, we find no evidence for a significant periodic signal on a time-scale of days. These time-scales are interesting because the roughly correspond to the expected frequency of maximum power for asteroseismic oscillations. This frequency is defined by

$$\nu_{\rm max} = \nu_{\rm max,\odot}\left(\frac{g}{g_\odot}\right)\left(\frac{T_{\rm eff}}{T_{\rm eff,\odot}}\right)^{-1/2}, \quad \text{(B1)}$$

where $\nu_{\rm max,\odot} = 3100\,\mu$Hz, $T_{\rm eff,\odot} = 5777$ K, and $g_\odot = 2.7 \times 10^4$ cm^2 s^{-1} (Brown et al. 1991; Kjeldsen & Bedding 1995). Given the spectroscopic parameters in Section 4.1, we estimate that $\nu_{\rm max} \approx 6.8\,\mu$Hz, which corresponds to a period of $P_{\rm osc} \approx 1.7$ d. With no clear peaks in the periodogram of the existing *TESS* data, we cannot presently use asteroseismology as an additional probe of the mass of the giant, but this may change with further analysis and additional *TESS* data.

Finally, many compact-object systems (e.g. Wagner et al. 1992; Zurita, Casares & Shahbaz 2003; Shahbaz et al. 2013) show rapid variability on time-scales of minutes to hours. We used the ROAD telescope (Hambsch 2012) to continuously observe the system for about 2 h on multiple nights, obtaining in total more than 3000 10-s *B*-band exposures. We have reduced these data using the ASAS-SN version of the Alard (2000) image subtraction software. We do not find any evidence for short (<1 h) time-scale *B*-band variability, with the rms scatter during individual nights below 0.01 mag. Given that the 'second light' contribution to the total *B*-band flux of V723 Mon is about 60 per cent, this translates to the short time-scale variability of this component being less that ∼2 per cent. However, on longer time-scales of hours to days *B*-band variability at the ∼2 per cent level is still possible (on top of the observed ellipsoidal modulations discussed in Section 4.3).

[1]*Department of Astronomy, The Ohio State University, 140 West 18th Avenue, Columbus, OH 43210, USA*
[2]*Center for Cosmology and Astroparticle Physics, The Ohio State University, 191 W. Woodruff Avenue, Columbus, OH 43210, USA*
[3]*Leibniz Institute for Astrophysics Potsdam (AIP), An der Sternwarte 16, D-14482 Potsdam, Germany*
[4]*Institute for Astronomy, University of Hawai'i, 2680 Woodlawn Drive, Honolulu, HI 96822, USA*
[5]*Vereniging Voor Sterrenkunde (VVS), Oostmeers 122 C, B-8000 Brugge, Belgium*

[6]*Bundesdeutsche Arbeitsgemeinschaft für Veränderliche Sterne e.V. (BAV), Munsterdamm 90, D-12169 Berlin, Germany*
[7]*American Association of Variable Star Observers (AAVSO), 49 Bay State Road, Cambridge, MA 02138, USA*
[8]*Núcleo de Astronomía de la Facultad de Ingeniería y Ciencias, Universidad Diego Portales, Av. Ejército 441, Santiago, Chile*
[9]*Millennium Institute of Astrophysics, Santiago, Chile*
[10]*School of Physics, The University of Melbourne, Parkville, VIC 3010, Australia*
[11]*ARC Centre of Excellence for All Sky Astrophysics in 3 Dimensions (ASTRO 3D)*
[12]*Department of Astronomy and Astrophysics, University of California, Santa Cruz, CA 95064, USA*
[13]*Department of Physics and Astronomy and Pittsburgh Particle Physics, Astrophysics and Cosmology Center (PITT PACC), University of Pittsburgh, 3941 O'Hara Street, Pittsburgh, PA 15260, USA*
[14]*Department of Astronomy, California Institute of Technology, Pasadena, CA 91125, USA*
[15]*Department of Astronomy, University of California Berkeley, Berkeley CA 94720, USA*
[16]*Centre for Astrophysics, University of Southern Queensland, Toowoomba, QLD, Australia*
[17]*Sydney Institute for Astronomy (SIfA), School of Physics, University of Sydney, NSW 2006, Australia*
[18]*Stellar Astrophysics Centre, Department of Physics and Astronomy, Aarhus University, DK 8000 Aarhus C, Denmark*

This paper has been typeset from a TEX/LATEX file prepared by the author.